A Proposal to Jefferson Lab PAC53

Measurement of the Two-Photon Exchange Contribution in Electron-Neutron and Positron-Neutron Elastic Scattering

E. Fuchey (spokesperson), D. Armstrong, T. Averett, M. Satnik, and Z. Wertz
William and Mary, Williamsburg, Virginia 23185, USA

S. Alsalmi (spokesperson)
King Saud University, Riyadh 11451, Saudi Arabia

P. Datta (spokesperson)
Lawrence Berkeley National Lab, Berkeley, California 94720, USA

B. Wojtsekhowski, A. Camsonne, C.-H. Leung, M. McCaughan, and A. Tadepalli
Thomas Jefferson National Accelerator Facility, Newport News, Virginia 23606, USA

C. Ayerbe Gayoso
Old Dominion University, Norfolk, Virginia 23529, USA

P. Blunden
Univeristy of Manitoba, Winninpeg, Canada

J. Boyd, N. Liyanage, M. Nycz, and A. Rathnayake
University of Virginia, Charlottesville, Virginia 232904, USA

D. Hamilton and R. Montgomery
SUPA School of Physics and Astronomy,
University of Glasgow, Glasgow G12 8QQ, UK

A. Hoghmrtsyan, H. Mkrtchyan, M. Mkrtchyan, A. Shahinyan, and V. Tadevosian
A.I. Alikhanyan National Science Laboratory (Yerevan Physics Institute), Yerevan 0036, Armenia

N. Kalantarians
Virginia Union University, Richmond, Virginia 23220, USA

W. Li
Mississippi State University, Mississippi State, MS 39762, USA

P. Markowitz
Florida International University, Miami, FL 33199, USA

R. Marinaro
Christopher Newport University, Newport News, Virginia, USA 23606

K. Nagai
The University of Memphis, Memphis, Tennessee 38152, USA

A.J.R. Puckett and S. Seeds
University of Connecticut, Storrs, Connecticut 06269, USA

A. Schmidt
George Washington University, Washington, District of Columbia 20052, USA

E. Voutier
Université Paris-Saclay, CNRS/IN2P3, IJCLab, 91405 Orsay, France

and the PWG collaboration.

(Dated: April 29, 2025)

Executive Summary

We propose to make a high precision measurement of the two-photon exchange contribution (TPE) in elastic positron-neutron and electron-neutron scattering at three four-momentum transfers Q^2 of 3.0, 4.5, and 5.5 $(\mathrm{GeV/c})^2$. This measurement purports to complete and extend the measurement of the two-photon exchange in electron-neutron scattering submitted to and approved by PAC48 in 2020, and recorded in 2022 (experiment E12-20-010, currently under analysis). This program means to address the open question of the discrepancy between G_E/G_M ratios measured in elastic electron-nucleon scattering via Rosenbluth separation on the one hand and polarization transfer on the other hand, often explained by a different sensitivity of each of the experimental methods to the TPE contribution. The measurement of the positron-neutron over electron-neutron cross section ratio provides a direct access to the TPE contribution, which can be compared to the discrepancy between Rosenbluth slope measurements and polarization measurements to determine the actual contribution of the TPE to this discrepancy.

The proposed experiment shall be performed with the Super BigBite Spectrometer (SBS), combined with the BigBite (BB) spectrometer, installed in Hall C, and using the proposed positron beam upgrade for CEBAF. It will measure simultaneous neutron and proton elastic scattering off deuterium, with positrons and with electrons, at two beam energies of 3.3 and 4.4 GeV for $Q^2 = 3.0$ $(\mathrm{GeV/c})^2$, and 4.4 and 6.6 GeV for $Q^2 = 4.5$ $(\mathrm{GeV/c})^2$ and $Q^2 = 5.5$ $(\mathrm{GeV/c})^2$. For each of the measured Q^2 values, the combination of electron and positron data sets will provide positron/electron neutron cross section ratios $R^n_{2\gamma}$; the combination of different energy datasets will provide Rosenbluth slope measurements on electrons and positrons. Using the maximum proposed intensity of 1 μA for unpolarized positrons, as well as 1 μA for electrons, this measurement requires 28 days (14 on positrons plus 14 on electrons) on a 15 cm cryogenic deuterium target, 12 days (6 on positrons plus 6 on electrons) on a 15 cm cryogenic hydrogen target for calibrations and monitoring of our equipment, distributed on all six settings, and 11 extra calendar days for kinematic changes and accelerator reconfiguration for positron and electron changes. The analysis of the proposed experiment will greatly benefit on the return of experience of the ongoing analysis of E12-20-010.

I. INTRODUCTION

In 1950s, a series of experiments performed by R. Hofstadter [1] revealed that nucleons have a substructure (which corresponds to our modern view in terms of quarks and gluons). The experiment confirmed M. Rosenbluth's theory of electron scattering [2] based on the one-photon exchange approximation. In this so-called Born approximation, where the interaction between the electron and the nucleon occurs *via* an exchange of one virtual photon (OPE), the unpolarized $e-N$ elastic cross section can be parameterized in terms of a nucleon magnetic, G_{M}, and electric, G_E, form factors. These form factors describe the deviation from a point-like scattering cross section, σ_{Mott}:

$$\left(\frac{d\sigma}{d\Omega}\right)_{eN\to eN} = \frac{\sigma_{Mott}}{\epsilon(1+\tau)} \left[\tau \cdot G_{M}^{2}(Q^2) + \epsilon \cdot G_{E}^{2}(Q^2)\right], \tag{1}$$

where E and E' are the incident and scattered electron energies, respectively, θ is the electron scattering angle, $\tau \equiv -q^2/4M^2$, with $-q^2 \equiv Q^2 = 4EE' \sin(\theta/2)$ being the negative four-momentum transfer squared, M is the nucleon mass, and $\epsilon = \left[1+2(1+\tau)\tan^2(\theta/2)\right]^{-1}$ is the longitudinal polarization of the virtual photon. We define the reduced cross section as the total cross section divided by the Mott Cross section:

$$\sigma_r \equiv \left(\frac{d\sigma}{d\Omega}\right) \cdot \frac{\epsilon(1+\tau)}{\sigma_{Mott}} = \tau \cdot G_{M}^{2}(Q^2) + \epsilon \cdot G_{E}^{2}(Q^2) \ = \ \sigma_{T} + \epsilon \cdot \sigma_{L}, \tag{2}$$

where σ_L and σ_T are the cross sections for longitudinally and transversely polarized virtual photons, respectively.

The linear ϵ dependence of the cross section is due to the σ_L term. The ratio σ_L/σ_T is the so-called Rosenbluth slope related to $\mathrm{G}_E/\mathrm{G}_M$(in OPE), see Fig. 1. The fits of world data displayed in this figure show a strong disagreement between the $\mathrm{G}_E^p/\mathrm{G}_M^p$ ratio from Rosenbluth measurements on the proton (shown as the solid line on Fig. 1) and the $\mathrm{G}_E^p/\mathrm{G}_M^p$ ratio from polarization transfer measurements (shown as the blue dot-dashed line in Fig. 1).

The nucleon electromagnetic form factors can reveal a lot of information about the nucleon internal structure, as well as the quark distribution. The form factors depend only on Q^2,

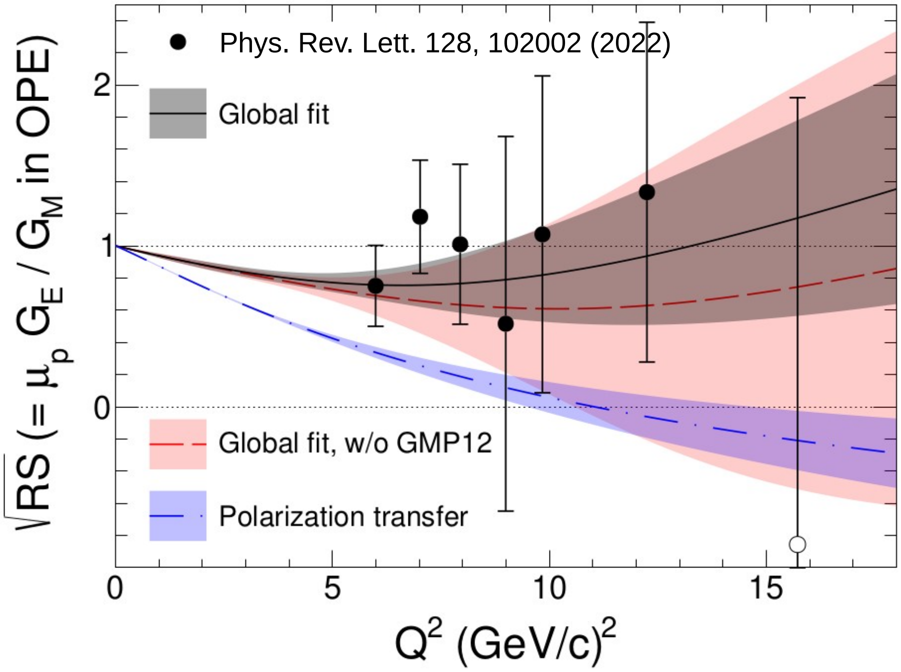

FIG. 1. The square root of Rosenbluth slope, corrected for kinematical factor $\sqrt{\tau}$ and μ_p, observed in elastic electron-proton scattering, adapted from Ref. [3]. The black markers show the latest Rosenbluth slope measurements from Ref. [3]. The black and red curves shows the global fit of Rosenbluth measurements at high Q^{2}respectively with and without the data published in [3]. The blue curve shows the global fit of polarization transfer. Note: since this global fit includes mostly data in the Q^2 range of 1 to 8.8 (GeV/c)^2, the global Rosenbluth slope fit does not represent well the very low Q^2 of 1 (GeV/c)^2.

defined earlier. In the limit of large Q^2, perturbative QCD (pQCD) provides well-motivated predictions for the Q^2-dependence of the form factors and their ratio, which is predicted to be independent of Q^2 (scaling). Studies show that pQCD validity will require a very large Q^2 of the order of 100 (GeV/c)^2 [4–6]. It was discovered at JLab, using the double polarization methods, that the proton electric and magnetic form factors behave differently starting at Q^2 $\approx$ 1 (GeV/c)^2. Experimentally, the nucleon form factors can be measured using one of two techniques: the polarization transfer technique and the aforementioned Rosenbluth technique. The polarization method examines the polarization transfer from longitudinally polarized electron to the recoiling nucleon and determine the resulting azimuthal asymmetry distribution using a polarimeter. Alternatively, one can use a polarized electron beam and polarized target. In the Rosenbluth method, the electric and magnetic from factors can be separated by making two or more measurements with different ϵ values (*i.e.* different beam energies and angles), but with same Q^2 value. The Rosenbluth technique requires an accurate measurement of the cross section and suffers from large systematic uncertainties arising from several factors, for instance the need for a precise determination of the scattering angle. Additionally, for a measurement of the neutron form factors, accurate knowledge of the neutron detector efficiency is required, which is particularly hard to achieve. These uncertainties can be greatly reduced by measuring the ratio of $e-n$ and $e-p$ quasi-elastic cross sections.

When comparing the values of G_{E}^{p}/G_{M}^{p} obtained from both techniques, a significant discrepancy was observed (see Fig. 1). Such a discrepancy implies a potential problem in our understanding of the nucleon substructure. Many efforts were made to explain this effect, and it is believed that the inconsistency is due to the contribution of two-photon exchange (TPE) in $e-N$ elastic scattering process [7, 8], but, as we will discuss next, this remains an open debate.

One of the properties of TPE is its sensitivity to the lepton charge i.e. the respective TPE contributions to the cross section of e^-N and e^+N are of opposite size. Based on this, several experiments measured elastic cross section ratios $\sigma_{e^+p}/\sigma_{e^-p}$ ratios. Both meta analysis of old elastic e^+p/e^-p data [10] and more recent measurement of $R_{2\gamma} = \sigma_{e^+p}/\sigma_{e^-p}$ Q^2 up to 2 (GeV/c)^2 from Olympus [9] (shown on Fig 2) and CLAS [11] have not managed to evidence the existence of TPE beyond their respective experimental uncertainties.[1] Higher Q^2 measurements with positrons and electrons on the proton have been proposed for the future Jefferson Lab positron upgrade, including measurements of $R_{2\gamma}$ up to 10 (GeV/c)^2 on the proton with CLAS12 [13], and super-Rosenbluth measurements of the proton cross sec-

---

[1] While the discrepancy shown in Fig. 1 looks already quite sharp at modest Q^2 values, the global fit does note include very low Q^2 data from Mainz [12], which does not observe a significant discrepancy between Rosenbluth and polarization transfer data.

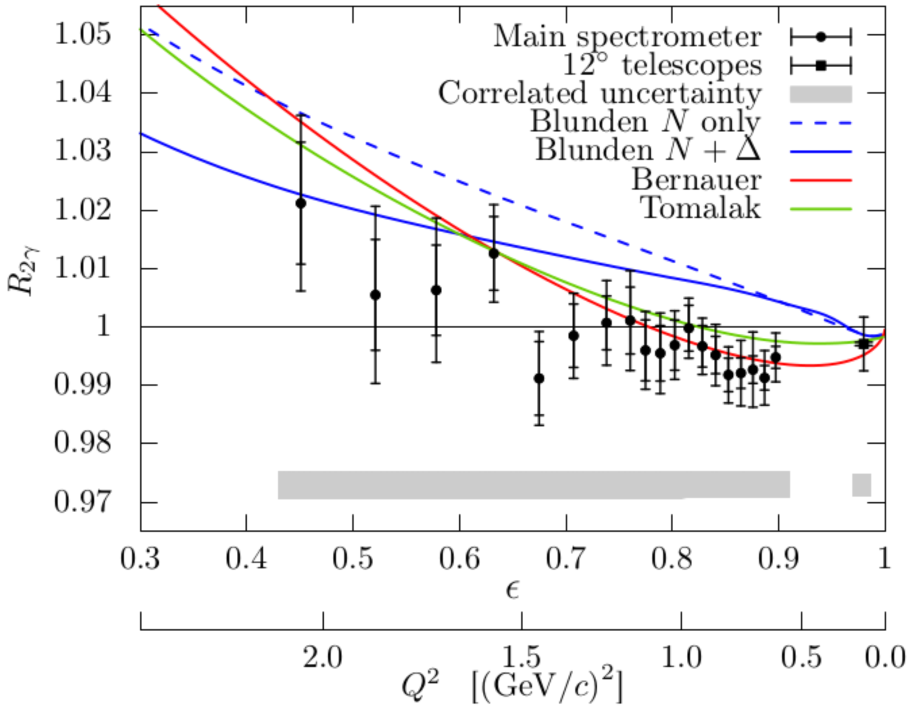

FIG. 2. Measurements of $R_{2\gamma} = \sigma_{e^+p}/\sigma_{e^-p}$ from Olympus [9] for Q^2< 2 (GeV/c)^2, showing the absence of a significant TPE contribution in this Q^2 range.

tion up to 5.5 (GeV/c)^2 in Hall C with HMS/SHMS [14]. Such measurements will greatly improve our understanding of the TPE contribution to the proton cross section.

While most neutron electric form factor measurements use a double polarization technique [15, 16] or a recoil polarization technique [17], the evaluation of the TPE contribution on the neutron remains important, as it may be a non-negligible correction to neutron form factor measurements such as the recently recorded GMn measurements in Hall A [18] and Hall B [19]. The experimental knowledge on the TPE contribution on the neutron is extremely reduced. The only experiment attempting to measure this quantity is the nTPE experiment E12-20-010 [20], which analysis is ongoing. This experiment performed a measurement of the Rosenbluth slope in e^-n at Q^2 = 4.5 (GeV/c)^2. While the analysis of this experiment (and especially the careful determination of the systematic uncertainties) is still ongoing, we believe that the comparison of this upcoming result with the existing SBS fit the upcoming polarization transfer measurement at $Q^2 = 4.5$ (GeV/c)^2 from GEn-RP [17] Predictions made for the electron-neutron case shown in Fig. 3, adapted from [21] shows a very modest contribution at lower Q^2, but growing significantly from $Q^2 = 3$ (GeV/c)^2 onwards. In

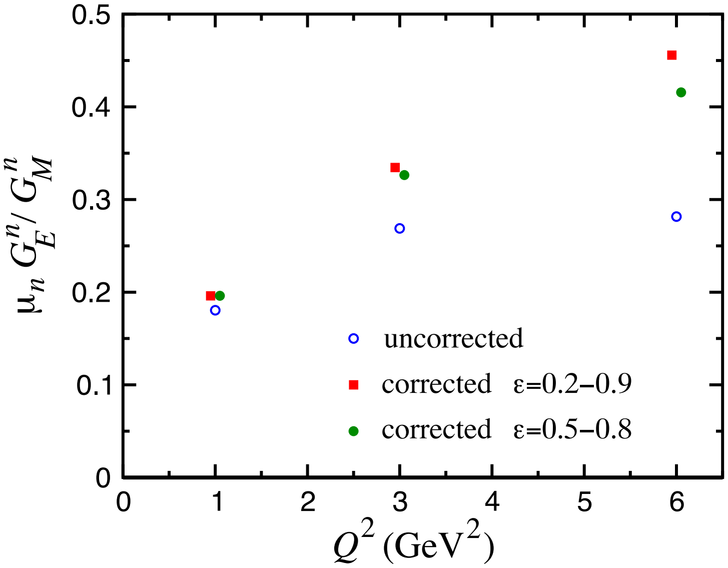

FIG. 3. Projected impact of TPE on G_E^n/G_M^n using LT separation, according to Ref. [21]. Blue hollow circles show old G_E^n/G_M^n polarization transfer measurements from [22]. Red solid squares show a *prediction* of this ratio with from a Rosenbluth measurement between $\epsilon = 0.2$ and $\epsilon = 0.9$. Green solid circles show a *prediction* of this ratio with from a Rosenbluth measurement between $\epsilon = 0.5$ and $\epsilon = 0.8$.

the following we propose to measure of the neutron TPE contribution with positron-neutron to electron-neutron cross section ratios $R^n_{2\gamma}$, along with Rosenbluth separated cross sections for both positron-neutron to electron-neutron quasi-elastic scattering, at three Q^2 values of 3, 4.5, and 5.5 (GeV/c)^2. The proposed measurements will test of the predictions from [21] and provide a very valuable insight on the TPE contributions in neutron form factor measurements.

II. PHYSICS MOTIVATION

A. Form factor measurements at high Q^2

The nucleon plays the same central role in hadronic physics that the hydrogen atom does in atomic physics and the deuteron in the physics of nuclei. The structure of the nucleon and its specific properties, such as charge, magnetic moment, size, mass; the elastic electron scattering form factors, resonances; and structure functions in DIS, are of fundamental scientific interest. Isospin is a fundamental property of the nucleon, so both the proton and neutron investigations are important to do. By using data on the proton and neutron form factors, the flavor structure could be explored [23]. It has already provided the most direct evidence for a diquark correlation in the nucleon [24–26].

Hadron structure, as seen in elastic electron scattering, in the one-photon exchange approximation, is defined by two functions of four momentum transfer square. They are: the helicity conserving Dirac form factor, F_1, which describes the distribution of the electric charge, and the helicity non-conserving Pauli form factor, F_2, which describes the distribution of the magnetic moment. These two form factors are the ingredients of the hadronic current. They contain information on the transverse charge distribution for an unpolarized and transversely polarized nucleon, respectively, in the infinite momentum frame [27, 28].

The Sachs form factors, G_E and G_M, the ratio of which will be extracted directly from the data, are related to F_1 and F_2 by

$$F_1 = \frac{G_E + \tau G_M}{1+\tau} \text{ and } F_2 = \frac{G_M - G_E}{\kappa(1+\tau)}, \tag{3}$$

where κ is the nucleon anomalous magnetic moment.

Already twenty-four years ago, an important development in QCD phenomenology has been the exploration of the generalized parton distribution (GPD) formalism [29–31], which provides relations between inclusive and exclusive observables. The nucleon elastic form factors F_1 and F_2 are given by the first moments of the GPDs

$$F_1(t) = \sum_q \int_0^1 H^q(x,\xi,t,\mu)dx \;\text{ and }\; F_2(t) = \sum_q \int_0^1 E^q(x,\xi,t,\mu)dx, \tag{4}$$

where H^q and E^q are two of the generalized parton distributions, x is the original momentum fraction of the parton x, ξ is the "skewdness" of the reaction[2] , t is the four-momentum transferred by the electron, μ is a scale parameter necessary for the evolution over Q^2, analogous to DIS parton distributions, and the sum is over all quarks and anti-quarks. GPDs may be accessed through processes such as deeply virtual Compton scattering, where the interaction is factorized into a hard part with the virtual photon/photon interactions with an individual quark and a soft part of the residual system where the GPD information is contained.

A fundamental nucleon feature, the spin, is related to GPDs, as shown by X. Ji [30]. The moments of GPDs can yield information, according to Ji's Angular Momentum Sum Rule, on the contribution to the nucleon spin from quarks and gluons, including both the quark spin and orbital angular momentum.

At present, experimental measurements of GPDs are still scarce. Until high Q^2 DVCS data becomes available, work has been done to attempt to parameterize these GPDs, which rely heavily on data from electromagnetic form factors and parton distributions from DIS as constraints [32]. Data at high Q^2 for G_E^n would contribute significantly in the development of these models. As we presented above, nucleon elastic form factors provide important input for the modeling of GPDs. At the same time, the measured cross section of elastic $e-p$ scattering at high Q^2 is significantly larger than predicted by Born-approximation calculations [33], indicating that TPE effects play a critical role in the high-Q^2 region and therefore must be well understood before conclusions about GPDs can be drawn.

B. The role of two-photon exchange in form factors

As we presented above, the form factors are important components for the study of the nucleon structure. However, the puzzle of the form factor ratio G_E/G_M at higher Q^2 partly blurs our understanding of the measurements. Such an observation underlines the importance of the understanding of the two-photon exchange for hadron physics.

---

[2] $-x \leq \xi \leq x$ get integrated with the integration on x

There are two different contributions of the two photon-exchange. The first one is the "soft" two-photon exchange, where one of the photons energy is very small compared to the other, which is usually included in radiative correction calculations such as those of Mo and Tsai [34]. This soft contribution being calculated in radiative corrections prescriptions and corrected for in our cross sections, it is not the subject of our measurement. The "hard" two-photon exchange, where both photons have a significant energy, and that we intent to measure, is the contribution remaining after the "soft" radiative corrections have been applied. The leading order contribution of the two-photon exchange to the elastic lepton-nucleon scattering is the interference term between the one-photon amplitude term $\mathcal{M}_{1\gamma}$ and the two-photon amplitude term $\mathcal{M}_{2\gamma}$:

$$\sigma_{eN} \propto |\mathcal{M}_{1\gamma}|^2 \pm 2\Re e[\mathcal{M}_{1\gamma}\mathcal{M}_{2\gamma}]. \tag{5}$$

This interference term depends on the cube of the charge of the lepton involved, *i.e.* at first order the sign of the two-photon exchange contribution is naively expected to flip from $e^- - N$ to $e^+ - N$. This means that the deviation from 1 of the ratio of quasi-elastic cross sections $R^N_{2\gamma} = e^+ - N/e^- - N$ is directly proportional to the TPE contribution. This statement above does not account for the interference of lepton- hadron-bremsstrahlung which also contributes to the ratio of positrons/electrons cross section. However, this contribution can be calculated and corrected for using the appropriate radiative correction prescriptions which do not neglect this contribution such as [34, 35]. In addition, the comparison between G_E/G_M from $e^+ - N$ Rosenbluth measurements, $e^- - N$ Rosenbluth measurements, and G_E/G_M from polarization transfer measurements will allow to test more effectively whether the difference between the latter two (observed for the proton, to be confirmed for the neutron) is due solely to the TPE. The measurement presented in this document proposes to measure the ratio of positron-neutron to electron-neutron quasi-elastic cross-section $R^n_{2\gamma}$, which is directly proportional to the two-photon exchange contribution:

$$R^n_{2\gamma} = \frac{\sigma_{e^+n}}{\sigma_{e^-n}}. \tag{6}$$

This simple and straightforward measurement is combined with a measurement of the Rosenbluth slope in electron- and positron-neutron scattering. Combined with the upcoming result on electron-neutron scattering from nTPE experiment E12-20-010 under analysis and compared to the upcoming GEN and GEn-RP measurements of G_E^n with polarization techniques, will provide an independent estimation of the two-photon exchange in neutron quasi-elastic scattering.

III. TECHNIQUE

This proposal uses the same instrumentation, simulation, and analysis development as the past GMn/nTPE experiments (E12-09-019/E12-20-010) [18, 20]. The GMn/nTPE experiments are one of several form factor experiments using the Super BigBite Spectrometer (SBS), and have run during Fall 2021 and Winter 2022.

The neutron form factors are challenging to be determine experimentally especially because there is no free neutron target. However, since deuterium is a loosely bound system, it can be viewed as the sum of a proton target and a neutron target. In fact, quasi-elastic scattering from deuterium has been used to extract the neutron magnetic form factor, G_M^n, at modestly high Q^2 for decades [36, 37] in single arm (e,e') experiments. In those experiments, the proton cross section needs to be subtracted by applying a single-arm quasi-elastic electron-proton scattering. This "proton-subtraction" technique suffers from a number of systematic uncertainties e.g. contributions from inelastic and secondary scattering processes.

Many years ago, L. Durand [38] proposed the so-called "ratio-method" based on the measurement of both $D(e,e'n)$ and $D(e,e'p)$ reactions. In this method, many of the systematic errors are canceled out. Several experiments [39–41] have applied the ratio-method to determine the neutron magnetic form factor.

This measurement will record simultaneous $D(e,e'n)$ and $D(e,e'p)$ reaction with electron beams and positron beams. The measurement with each beam ($e^{\pm}$) provides the ratio R' of neutron over proton yields:

$$R'_{n/p} = \frac{N_{e,e'n}}{N_{e,e'p}} \tag{7}$$

$R'_{n/p}$ needs to be corrected to extract the ratio of quasi-elastic scattering cross section ratio from nucleons $R_{n/p}$:

$$R_{n/p} = \frac{\sigma_{en}}{\sigma_{ep}} = f_{corr} \times R'_{n/p}, \tag{8}$$

where the correction factor f_{corr} takes into account the hadron efficiencies, the radiative corrections, the absorption in path from the target to the detector, and small re-scattering correction. Measurements of $R_{n/p}$ for positron and electrons provide the positron-over-electron super-ratio $\rho_{\pm}$ which depends directly on $R^n_{2\gamma}$ and $R^p_{2\gamma}$

$$\rho_{\pm} = \frac{\sigma_{e^+n}}{\sigma_{e^+p}} / \frac{\sigma_{e^-n}}{\sigma_{e^-p}} = \frac{R^n_{2\gamma}}{R^p_{2\gamma}} \tag{9}$$

Our measurement of the super-ratio $\rho_{\pm}$ combined with the projected CLAS measurements of $R^p_{2\gamma}$ proposed to PAC51 [13] approved allows to straightforwardly obtain $R^n_{2\gamma}$:

$$R^n_{2\gamma} = \rho_{\pm} \times \left(R^p_{2\gamma}\right)_{Meas} \tag{10}$$

Our experiment also plans to measure $R_{n/p}$ at the same Q^2 and different beam energies provides a way to access the Rosenbluth slope of quasi-elastic electron-neutron and positron-neutron cross section. Applying the Rosenbluth technique from the measurement of the absolute $e-n$ cross section to measure G$^n_{_E}$ requires a very accurate measurement of the cross section and suffers from large uncertainties. Extracting the value of G$^n_{_E}$ from the ratio of quasi-elastic yields, $R_{n/p}$ from a deuteron target allows us to overcome this issue. The nTPE experiment [20] has taken elastic $e^- - n$ scattering at Q^2 =4.5 (GeV/c)^2 and two beam energies to measure the Rosenbluth slope and extract (in OPE approximation) the neutron electric form factor, G$^n_{_E}$, at one value of momentum transfer. This new experiment also proposes to perform a similar measurement with positrons at the same Q^{2}and two additional Q^2 values of 3 and 5.5 (GeV/c)^2.

Writing $R_{n/p}$ at two values of ϵ using $S^{n(p)} = \sigma^{n(p)}_{_L} / \sigma^{n(p)}_{_T}$ as:

$$R_{n/p,\ \epsilon_1} = \frac{\epsilon_1 \sigma^n_{_L} + \sigma^n_{_T}}{\epsilon_1 \sigma^p_{_L} + \sigma^p_{_T}} \qquad R_{n/p,\ \epsilon_2} = \frac{\epsilon_2 \sigma^n_{_L} + \sigma^n_{_T}}{\epsilon_2 \sigma^p_{_L} + \sigma^p_{_T}}$$

In these two equations there are two unknown variables: $\sigma^n_{_L}$ and $\sigma^n_{_T}$. We remind here that proton and neutron measurements are made simultaneously with the same apparatus. Thanks to this, the dominant contribution to the uncertainty of the Rosenbluth slope of the reduced cross section vs. ϵ, $S^n = \sigma_{_L}^n/\sigma_{_T}^n$, will come from the uncertainty of S^p. The resulting equation for S^n is:

$$A = B \times \frac{1+\epsilon_1 S^n}{1+\epsilon_2 S^n} \approx B \times (1 + \Delta\epsilon \cdot S^n),$$

with $\Delta\epsilon = \epsilon_1 - \epsilon_2$, and where the variable $A = R_{n/p,\epsilon_1}/R_{n/p,\epsilon_2}$ will be measured with statistical precision of 0.1%. Assuming, for this estimate, equal values of Q^2 for two kinematics, the τ and $\sigma_{_T}$ for two kinematics are canceled out, and the variable B depends on the proton Rosenbluth slope S^p:

$$B = (1+\epsilon_2 S^p)/(1+\epsilon_1 S^p) \tag{11}$$

For electron measurements, the current knowledge of the $e^- - p$ elastic scattering cross section obtained in the single arm H(e,e')p and H(e,p)e' experiments, compiled in the latest global analysis of $e-p$ cross section [3], will be also used for precision determination the experiment kinematics at 3, 4.5, and 5.5 (GeV/c)^2. For positron measurements, we may rely on the positron-proton Rosenbluth slope measured from the Super-Rosenbluth experiment proposed in Hall C at PAC51 [14].

For actual small range of ϵ and small value of the slope, $B \approx (1 - \Delta\epsilon \cdot S^p)$. We note here onwards $S^n_\pm$ the Rosenbluth slope for $e^\pm n$. In the simplest model, the Rosenbluth slope $S^n_\pm$ is a sum of the slope due to $\mathrm{G}^n_{_E}/\mathrm{G}^n_{_M}$ and the neutron two-photon exchange contribution to the Rosenbluth slope S^{TPE} (under the hypothesis that the polarization transfer measurements aren't affected by TPE):

$$S^n_\pm = (G^n_E/G^n_M)^2/\tau \mp S^{\mathrm{TPE}}, \tag{12}$$

From which the extraction of S^{TPE} becomes straightforward:

$$S^{\mathrm{TPE}} = \mp(S^n_\pm - (G^n_E/G^n_M)^2/\tau), \tag{13}$$

or, combining both measurements:

$$S^{\mathrm{TPE}} = (S^n_- - S^n_+)/2. \tag{14}$$

This value of S^{TPE} can then be compared to the value of nTPE obtained with Eq. 10. The uncertainties for these measurements are discussed in the section dedicated to systematic uncertainties.

IV. PROPOSED MEASUREMENTS AND EXPERIMENTAL SETUP

We propose to use the same experimental setup of the past E12-09-019/E12-20-010 experiments. We have three Q^2 values with two beam energy each: $Q^2 = 3.0$ $(GeV/c)^2$ at 3.3 GeV/1.5 pass and 4.4 GeV/2 pass), $Q^2 = 4.5$ $(GeV/c)^2$ at 4.4 GeV/2 pass and 6.6 GeV/3 pass, and $Q^2 = 5.5$ $(GeV/c)^2$ at 4.4 GeV/2 pass and 6.6 GeV/3 pass, obtaining two ϵ values for each Q^2 value. Each of these kinematics will be run with both unpolarized positron beams and unpolarized electron beams, at the maximum intensity available for unpolarized positrons in Hall C, *i.e.* 1 μA. Using the same intensity for positrons and electrons will minimize the uncertainties associated with the luminosity for the ratio $\rho_\pm = R^{e+}_{n/p}/R^{e-}_{n/p}$. This will allow us to measure:

- the super ratio of quasi-elastic neutron/proton cross section ratios for positrons and electrons;
- the effective Rosenbluth slope for positrons and electrons.

Table. I displays the kinematic settings of the proposed experiment.

Kinematic	e^+/e^- - I_{beam} (μA)	Q^2 $(GeV/c)^2$	E (GeV)	E$'$ (GeV)	θ_{BB} degrees	p' (GeV/c)	θ_{SBS} degrees	ϵ
1+/-	$e^{+/-}$ (1.0)	3.0	3.3	1.71	42.8	2.35	29.5	0.638
2+/-	$e^{+/-}$ (1.0)	3.0	4.4	2.81	28.5	2.35	34.7	0.808
3+/-	$e^{+/-}$ (1.0)	4.5	4.4	2.00	41.9	3.20	24.7	0.600
4+/-	$e^{+/-}$ (1.0)	4.5	6.6	4.20	23.3	3.20	31.2	0.838
5+/-	$e^{+/-}$ (1.0)	5.5	4.4	1.47	54.9	3.75	18.7	0.420
6+/-	$e^{+/-}$ (1.0)	5.5	6.6	3.67	27.6	3.76	26.9	0.764

TABLE I. Kinematic settings of the proposed experiment.

A. Experimental Setup

This experiment will study electron scattering from a 15 cm long liquid Deuterium target held in a vacuum. The scattered electron will be detected in the BigBite spectrometer as configured for GMn/nTPE E12-09-019/E12-20-010. This configuration for the proposed experiment will be strictly the same as the configuration for GMn/nTPE and includes:

- GEM detectors for a 1% momentum resolution tracking;
- a lead glass preshower and shower for trigger, energy measurement, and PID;
- a Cherenkov detector for pion rejection;
- an hodoscope for optimize timing resolution.

The neutron arm is arranged with a dipole magnet 48D48 (SBS) and a segmented sampling hadron calorimeter (HCal) to detect and reconstruct the hadron position. The SBS magnet sweeping quasi-elastic protons upwards, the comparison between the expected position of the reconstructed hadron allows to separate protons and neutrons as illustrated in Fig. 4. This setup is identical to the GMn/nTPE experiment setup which ran succesfully in 2021/2022 and will be installed in Hall C. The experimental setup installed in Hall C is illustrated in Fig. 5. More details on the experimental setup have been put on Appendix A. The SBS spectrometer was funded by DOE with large contributions provided by the collaborating institutions from USA, Italy, UK, and Canada.

B. Running conditions for this experiment compared to E12-20-008

This section will compare the running conditions for the proposed experiment with the running conditions for GMn/nTPE experiment E12-20-008.

a. BigBite and SBS in Hall C GMn/nTPE was run in Hall A, which features the largest floor space/clearance. Provided the future experimental program of Hall A with the Moller [42] experiment followed up by SoLID [43], we have decided to propose this experiment in Hall C. One of the main potential issues would be the lack of space in Hall C.

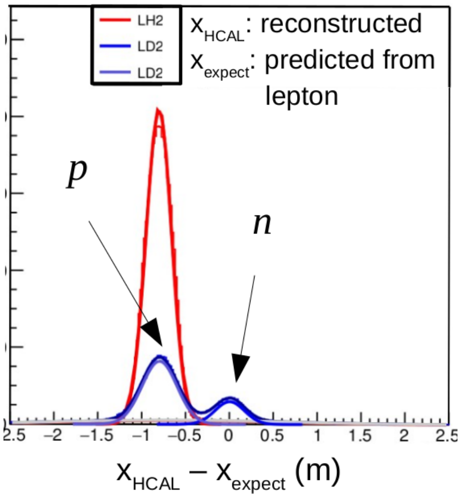

FIG. 4. Distribution of difference between the position expected in HCal (from the electron information) x_{expect} and the reconstructed position in HCAL x_{HCal}, for hydrogen data (red) and deuterium data (blue) evidencing the proton (shifted upwards *i.e.* negative in transport coordinates) and neutron peaks (centered at zero).

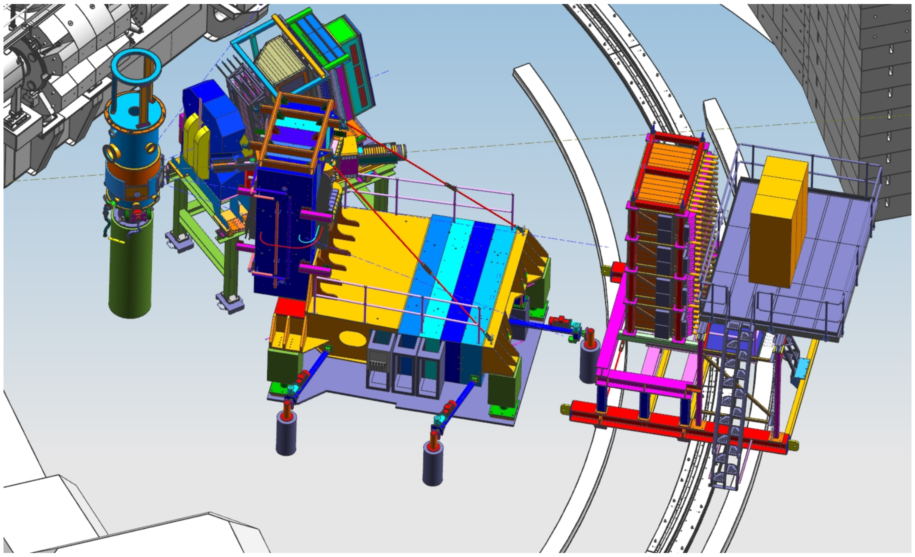

FIG. 5. Layout of the experimental setup, including the BigBite spectrometer, the SBS magnet, and the Hadron Calorimeter (HCal) in Hall C. The HMS and SHMS do not participate to the measurement and are pushed back to their maximum angle.

The Hall C engineering team checked for us that the different setups we will require will not interfere with the HMS and SHMS once pushed back to their largest angle. Hall C being equipped with a overhead crane, we do not anticipate any additional difficulty changing settings compared to Hall A.

b. Beam intensity GMn/nTPE was originally planned to run at 30 μA. Due to issues with the GEMs explained in Appendix A and resolved since, GMn/nTPE run at a fraction of this current, from 5 to 10 μA. In the experiment we propose, the beam intensity will be limited to 1 μA by the maximum intensity for the positron beam. The trigger rates and detector occupancies which were handled by the detectors during the GMn/nTPE data taking at 5 to 10 μA will be down significantly, and will therefore be essentially a non-issue.

V. SYSTEMATIC UNCERTAINTIES

In this section the contributions to the systematic uncertainties for this experiment are listed and discussed. The uncertainties on the ratio of neutron-to-proton cross section ratios $R_{n/p}$ are discussed first. The uncertainties on the quantities of interest $R^n_{2\gamma}$ and S^n are discussed next.

A. Systematic uncertainties on $R_{n/p}$, $\rho_\pm$, A

A majority of the potential sources of systematic uncertainties (Fermi motion, nuclear corrections, accidentals, target density, etc) cancel in the ratio $R_{n/p}$, which is one of the strengths of this experimental method. The remaining systematic uncertainties from the experimental setup have been partially evaluated in the GMn/nTPE experiment. The sources of systematics include radiative corrections, HCal detection efficiency, inelastic contamination, and neutron-proton charge exchange in final state interactions (FSI). The evaluation of $R^n_{2\gamma}$ also includes an uncertainty on the luminosity to normalize the electron and positron data samples with respect to each other. The sources of uncertainties as well as their *preliminary* evaluation for each kinematic is provided in Table. II. The method to evaluate these is discussed in the next paragraphs. The errors for $\Delta\rho_\pm/\rho_\pm$ are calculated as such:

Q^2 ((GeV/c)^2)	3.0	4.5	5.5	$\delta_{cov,\ e+/e-}$	$\delta_{cov,\ \epsilon_1/\epsilon_2}$
Radiative corrections*	0.77	1.11	1.26	+0.80	0.0
Inelastic contamination	0.33	0.75	0.84	+0.5	0.0
Nucleon detection efficiency*	0.7	0.7	0.7	+0.95	+0.5
Nucleon charge exchange in FSI	0.04	0.01	0.02	+0.95	0.0
Selection stability	0.16	0.15	0.40	+1.00	0.0
$\Delta R_{n/p}$	1.10	1.52	1.72	-	-
$\Delta\rho_\pm/\rho_\pm$	0.44	0.74	0.83	-	-
$\Delta A/A$	1.40	2.03	2.32	-	-

TABLE II. *Estimated* and preliminary* contributions to the systematic error on $R_{n/p} = \sigma_{en}/\sigma_{ep}$ from the GMN analysis (in percent). The total systematic errors on $R_{n/p}$ is the quadratic sum of all other errors. We made the assumption that the systematics for the two beam energies for the same Q^2 are of similar size. $\delta_{cov,\ e+/e-}$ and $\delta_{cov,\ \epsilon_1/\epsilon_2}$ are the assumed correlation between the uncertainties for the e^+ and e^- measurements and the ϵ_1 and ϵ_2 measurements respectively. For the calculation of $\Delta\rho_\pm/\rho_\pm$ and $\Delta A/A$, we added all uncertainties accounting for the assumed correlations as described in equation 15.

$$\frac{\Delta\rho_\pm}{\rho_\pm} = \left(\sum_{corr}\left(\frac{\Delta R_{n/p}}{R_{n/p}}\bigg|_{corr}^{e^+}\right)^2 + \left(\frac{\Delta R_{n/p}}{R_{n/p}}\bigg|_{corr}^{e^-}\right)^2 + 2\,\frac{\Delta R_{n/p}}{R_{n/p}}\bigg|_{corr}^{e^+}\frac{\Delta R_{n/p}}{R_{n/p}}\bigg|_{corr}^{e^-}\left(1-\delta_{cov,\ e^+/e^-}\right)\right)^{1/2} \tag{15}$$

where “*corr*” is the considered correction (RC, inelastic, etc), and $\delta_{cov,\ e^+/e^-}$ is the correlation factor listed in Table II. $\Delta A/A$ would write similarly to Eq. 15 by substituting $\rho_\pm$ with A and $\delta_{cov,\ e^+/e^-}$ with $\delta_{cov,\ \epsilon_1/\epsilon_2}$. We discuss and justify the values of $\delta_{cov,\ e^+/e^-}$ and $\delta_{cov,\ \epsilon_1/\epsilon_2}$ for each of the corrections in their respective paragraphs.

a. Radiative corrections For the GMn/nTPE analysis, the radiative corrections have been included in the Monte Carlo samples generated with SIMC, which uses the radiative calculations by Mo and Tsai [34] *with peaking approximation*. This generator provides the option to include only the electron radiative tails for both $\mathrm{D}(e, e'p)$ and $\mathrm{D}(e, e'n)$ events, or to include electron radiative tails and proton radiative tails for $\mathrm{D}(e, e'p)$. The first case treats both proton and neutron as chargeless point particles, which represents an extreme case. The second case is more realistic, only treating the neutron as chargeless, but also neglects its structure. The systematic uncertainty is evaluated as the difference of $R_{n/p}$ obtained following each of these two prescriptions for $\mathrm{D}(e, e'p)$ and $\mathrm{D}(e, e'n)$ Monte Carlo samples.

As mentioned above, the radiative correction prescription implemented for SIMC applies the peaking approximation which essentially eliminates the contribution from the lepton-hadron bremsstrahlung interference. This can be considered somewhat satisfactory for the GMn measurement and to a lesser extent for the nTPE measurement. However, if not corrected for, the lepton-hadron bremsstrahlung interference becomes non-negligible in the $R_{2\gamma}$ ratio as other contributions cancel out. Fortunately, there are many other prescriptions available to correct for this effect, including Mo and Tsai *without* the peaking approximation, other prescriptions [35, 44]. While we quote and use the preliminary radiative corrections systematic uncertainty from the GMn analysis, we plan to extract Rn/p, $R^n_{2\gamma}$ and S^{TPE} with all models quoted above for our analysis. Combining the values of those quantities obtained with all radiative corrections prescriptions may reduce our systematic uncertainties by up to a factor two. The values quoted in Table II are the preliminary uncertainty extracted from the GMn/nTPE analysis divided by a factor three to account for the margin of progress that we potentially have.

Since most of the contributions from the radiative corrections cancel in the $\rho_\pm$ ratio, with the exception of the interference between lepton and hadron bremsstrahlung, we may therefore consider a correlation $\delta^{RC}_{cov,\ e^+/e^-}$ of 80% for the contribution to the radiative corrections. In the A ratio, since the incident and outgoing electron have different energies, the radiative corrections may not be correlated at all between each other. Therefore we set the correlation $\delta^{RC}_{cov,\ \epsilon_1/\epsilon_2}$ to zero.

b. Inelastic contamination The distribution of Monte Carlo generated $\mathrm{D}(e, e'p)$ and $\mathrm{D}(e, e'n)$ samples distributions in Δx are normalized to the LD2 data sample distribution in Δx, together with a distribution to model the inelastic contamination. This distribution can be an analytic function which parameters are fitted together with the normalization of the Monte Carlo samples to the LD2 data sample. Three different analytic functions have been considered: a two-order polynomial, a three-order polynomial, and a gaussian. The background function can also be a distribution of Δx of the same LD2 data sample with an ”anti-selection” applied on Δy (all other selection parameters being the same as for quasi-elastic selection) The last function combines an inelastic Monte Carlo sample generated using the Christy-Bosted parametrization [45], combined with a distribution of Δx of the same LD2 data sample with an anti-selection applied on Δt the time difference between HCal and BigBite. This parametrization, shown in 6 provides the best adjustment. The systematic uncertainty is provided by the standard deviation between all inelastic contamination functions.

Many channels contributing to the inelastic contamination bear a lepton charge dependence,

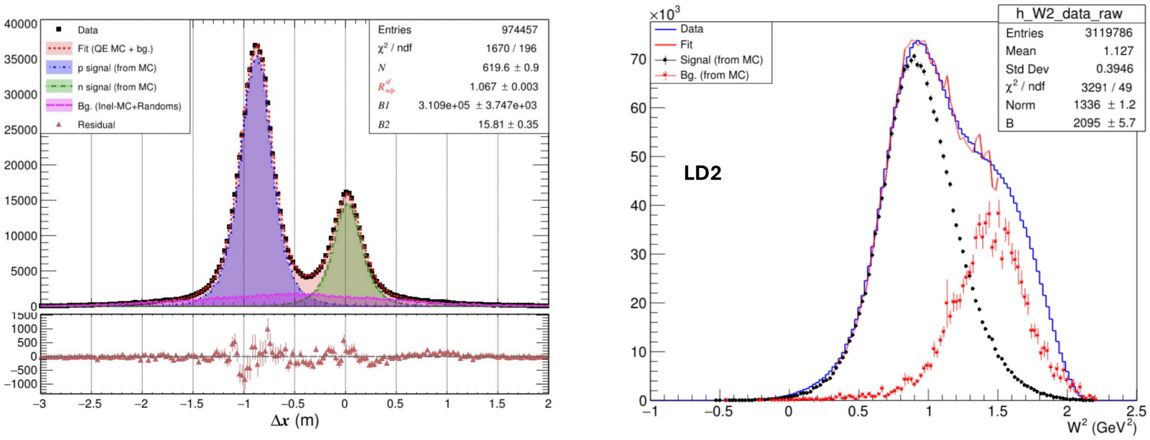

FIG. 6. Left: Global fit of Monte Carlo D$(e, e'p)$ (blue), D$(e, e'n)$ (green) and inelastic D$(e, e'X)$ inelastic Monte Carlo sample function, adjusted to the data (black markers). Right: LD2 data distribution in W^2 (blue), compared with D$(e, e'p)$ and D$(e, e'n)$ Monte Carlo samples (black) and D$(e, e'X)$ inelastic Monte Carlo sample (red).

therefore, we cannot assume a perfect cancellation of errors in the $\rho_\pm$ ratio. Nonetheless, correlation $\delta^{Inel}_{cov,\ e^+/e^-}$ of 50% for the contribution to the inelastic contamination in this ratio should be conservative. However, in the A ratio, since many parameters are different (beam energy, active HCal area) we anticipate a much smaller correlation $\delta^{Inel}_{cov,\ \epsilon_1/\epsilon_2}$ which we set to zero.

c. Nucleon detection efficiency The understanding of the HCal detection efficiency is one of the key parameters for this experiment. A full discussion of the HCal detection efficiency analysis is provided in Appendix B.

To summarize, there are several contributions to the neutron detection efficiency systematics. The first contribution comes from the HCal non-uniformity. It is estimated extracting $R_{n/p}$ with and without correcting for the non-uniformity (as described in 3), which bring a correction of 0.2 to 0.5%. The second contribution in the is the uncertainty on the uncertainty of proton detection efficiency due to inelastic contamination. This effect becomes significant in the GMn analysis at higher Q^2 of 7.5 (GeV/c)^{2}and beyond. At the Q^2we are considering, we estimate that this effect accounts for less that 0.2%. The third contribution comes from the gain variation of HCal. This gain variation can be kept in control by regularly taking LH_2 data to evaluate the relative response of HCal over time. The analysis from GMn/nTPE showed a very modest gain variation over the span of the data taking time. We also provision to take LH2 data with different SBS magnet settings to cover all the HCal coverage. We provision to take about one hour of LH_2 data for every three hours of LD_2 data on average. The last contribution comes from the absence of data sets to obtain direct neutron detection efficiency for HCal. This problem can be solved for the proposed experiment by requesting additional beamtime to perform a neutron detection efficiency measurement described in the next paragraph.

In the $\rho_\pm$ ratio, the kinematics are the exact same from one beam species to the other, therefore the HCal area involved in the measurement should be the same and the beam efficiency should in theory cancel entirely. We set the correlation $\delta^{HCal}_{cov,\ e^+/e^-}$ to 95% to account for small gain variations. In the A ratio, the HCal area involved in the detection is quite different from one kinematic to the other. Nevertheless, in the nTPE/E12-20-010, we observed a clear correlation of the HCal response between both kinematics. While we have yet to determine rigorously the actual correlation coefficient, we estimate that a correlation factor of 0.5 should be reasonable and achievable.

Neutron detection efficiency measurement Along with this new experiment, we will have a great opportunity to measure the HCal neutron detection efficiency to validate the neutron efficiency estimated by Monte Carlo. The elected channel for this measurement is $\gamma p \rightarrow \pi^+ n$. The LH2 target will be used, with 6% radiation length copper radiator mounted upstream to increase real photon generation. This will be combined with a 5μA intensity electron beam. The BigBite magnet polarity will be reversed to select π^+ and deflect electrons. This measurement can be performed with the "3-" kinematic setting *i.e.* Q^2= 4.5 (GeV/c)^2, low energy/2pass. Strict kinematic requirements on the pion and real photon reconstructed energy will be applied to select the $\gamma p \rightarrow \pi^+ n$. The selected kinematic allows to cover a sizeable fraction of the HCal surface, as shown on Fig 7. This data will used for the validation of the neutron detection efficiency with Monte Carlo, therefore it is not required to cover the entirity the HCal surface. Our simulation of $\gamma p \rightarrow \pi^+ n$ in the BigBite+SBS indicates that the rates of *clean* $\gamma p \rightarrow \pi^+ n$ is over 5000 per hour. A data taking of 16 hours (two shifts) at this setting will provide 80 thousands $\gamma p \rightarrow \pi^+ n$ events

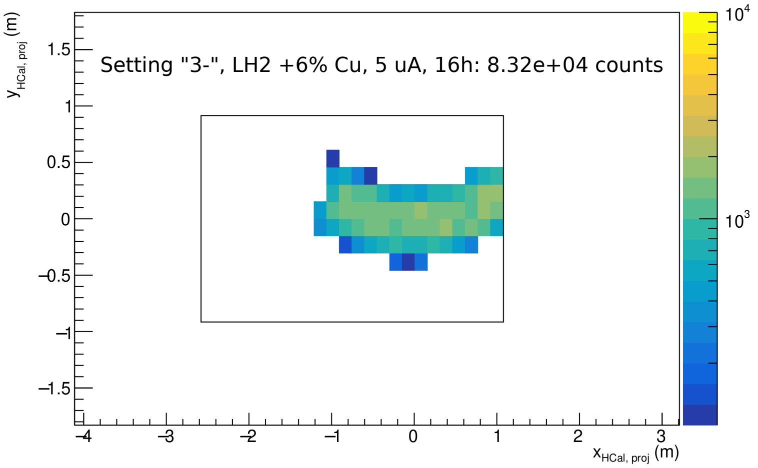

FIG. 7. Projected footprint and counting rates of $\gamma p \rightarrow \pi^+$(BigBite)n(HCal) for 16 hours of data taking at 5 μA on 15 cm LH$_2$ with 6% Cu radiator upstream, with the "3-" kinematic setting (Q^2= 4.5 (GeV/c)^2, low energy/2pass).

to estimate our calorimeter response to the neutron with a precision better than 0.4%. This measurement combined our existing and upcoming studies shall allow us to achieve an uncertainty on the HCal detection efficiency of the order of better than 0.7%. We do request an additional 16 hours of beam time with 5 μA on liquid hydrogen target combined with a 6% radiation length copper plate. This request is included in Table VII.

d. Nucleon charge exchange in FSI The symmetry of the deuterium nucleus means that the respective probabilities of charge exchange from proton-neutron and neutron-proton in FSI are expected to be mostly equal, and therefore the systematic uncertainty is expected to mostly cancel. The uncertainty on proton/neutron charge exchange had been provided to us by M. Sargsian [46]. According to his calculations, the effect should contribute to the cross proton and neutron section by less than 5%, and the uncertainty is better than 0.1%.

B. Systematic uncertainties on $R^n_{2\gamma}$

The systematic uncertainties contributing $R^n_{2\gamma}$ are compiled on Table. III. This table also

Q^2 ((GeV/c)^2)	3.0	4.5	5.5
$\Delta\rho_\pm/\rho_\pm$ (stat)	0.28	0.25	0.58
$\Delta\rho_\pm/\rho_\pm$ (syst)	0.44	0.74	0.83
$\Delta R^p_{2\gamma}/R^p_{2\gamma}$ [13]	0.78	0.42	0.79
$\Delta R^n_{2\gamma}/R^n_{2\gamma}$ (syst)	0.93	0.89	1.28

TABLE III. *Preliminary* contributions to the systematic error on $R^n_{2\gamma} = \sigma_{e^+n}/\sigma_{e^-n}$ (in percent). The total systematic errors on $R^n_{2\gamma}$ is the quadratic sum of all other errors.

provides the statistical accuracy for $\rho_\pm$. The calculations of the uncertainties on $\rho_\pm$ have been explained in Sec. V A and copied from Table II. In both this measurement and the Rosenbluth measurement, the luminosity does not directly play a role, as for each kinematic we measure a ratio of cross section which does not depend on the total integrated luminosity. The uncertainties on $R^p_{2\gamma}$ have been taken from the estimations from [13]. All these systematics have been added quadratically.

C. Systematic uncertainties on S^n

Table. IV lists the estimated contributions to systematic errors on the Rosenbluth slope measurement. The values and uncertainties for S^p come from the uncertainties of the data fits from the latest Rosenbluth publication from Christy *et al.* [3] for e^- and from the uncertainty estimations from [14] for e^+. The calculations of the uncertainties on $A = R^{\epsilon_1}_{n/p}/R^{\epsilon_2}_{n/p}$ have been explained in Sec. V A and copied from Table II. The error on ΔS^n writes:

$Q^2((GeV/c)^2)$	3.0 (e^-)	3.0 (e^+)	4.5 (e^-)	4.5 (e^+)	5.5 (e^-)	5.5 (e^+)
$\Delta A/A$ (stat, %)	0.32	0.32	0.40	0.40	0.58	0.58
$\Delta A/A$ (syst, %)	1.40	1.40	2.03	2.03	2.32	2.32
S^p [3, 14]	0.1056	-0.0267	0.0616	-0.0608	0.0478	-0.0773
ΔS^p [3, 14]	0.0160	0.0114	0.0165	0.0164	0.0170	0.0254
ΔS^n	0.100	0.096	0.103	0.103	0.087	0.094

TABLE IV. Estimated contributions to the statistical and systematic uncertainties on the measured Rosenbluth slopes for this experiment. The calculations of the total uncertainty is explained in the text.

$$\Delta S^n = 1/\Delta\epsilon(\Delta A/A + \Delta B/B^2 + ADSp/(1 - DeSp)2), \tag{16}$$

with $B = (1 + \epsilon_2 S^p)/(1 + \epsilon_1 S^p)$ and therefore $\Delta B = \Delta S^p \Delta\epsilon/(1 + \epsilon_1 S^p)$.

VI. PROJECTED RESULTS

A. Quasi-elastic counting rates

The signals for this experiment have been generated using the G4SBS elastic/quasi-elastic generator. We generated a reasonably large sample of quasi-elastic events N_{Gen} for each kinematics, within a solid angle $\Delta\Omega_{Gen}$ that was larger than the detector acceptance. To evaluate the detector solid angle, we define simple criteria that each event has to pass, defined as follows:

Point	Beam/ Target	Q^2 $(\mathrm{GeV/c})^2$	E_{beam} (GeV)	I_{beam} (μA)	n rates (Hz)	p rates (Hz)	beam time (h)	n counts ($\times$1000)	p counts ($\times$1000)
1+/-	$e^{+/-}$/LD2	3.0	3.3	1.0	2.55	7.44	24 × 2	220	643
1+/-	$e^{+/-}$/LH2	3.0	3.3	1.0	-	7.44	12 × 2	-	322
2+/-	$e^{+/-}$/LD2	3.0	4.4	1.0	4.00	11.67	16 × 2	230	672
2+/-	$e^{+/-}$/LH2	3.0	4.4	1.0	-	11.67	16 × 2	-	672
3+/-	$e^{+/-}$/LD2	4.5	4.4	1.0	0.49	1.54	96 × 2	169	532
3+/-	$e^{+/-}$/LH2	4.5	4.4	1.0	-	1.54	32 × 2	-	177
4+/-	$e^{+/-}$/LD2	4.5	6.6	1.0	0.94	3.11	48 × 2	162	537
4+/-	$e^{+/-}$/LH2	4.5	6.6	1.0	-	3.11	16 × 2	-	89
5+/-	$e^{+/-}$/LD2	5.5	4.4	1.0	0.186	0.541	120 × 2	80	234
5+/-	$e^{+/-}$/LH2	5.5	4.4	1.0	-	0.541	40 × 2	-	78
6+/-	$e^{+/-}$/LD2	5.5	6.6	1.0	0.576	1.980	36 × 2	75	256
6+/-	$e^{+/-}$/LH2	5.5	6.6	1.0	-	1.980	12 × 2	-	86

TABLE V. Quasi-elastic $e-n$ and $e-p$ counting rates, for each kinematic, proposed beam-on-target time and total statistics.

- require a primary track, going through all 5 GEM layers (electron arm);
- require non-zero energy deposit in both the preshower and shower (electron arm);

- require non-zero energy deposit in HCal (hadron arm).

The quasi-elastic data rates and statistics are compiled for both kinematics in Table. V, along with the respective beam currents, beam/targets, and running times. This table includes the measurements on LH2 meant for HCal gain and systematic studies. The background/trigger rates on top of which this signal will sit is discussed for the different kinematics in Appendix C.

B. Projected measurements

The projected results including statistics and systematic uncertainties for $R^n_{2\gamma}$ are presented for all kinematics on Fig. 8. The projected expected Rosenbluth slope measurement

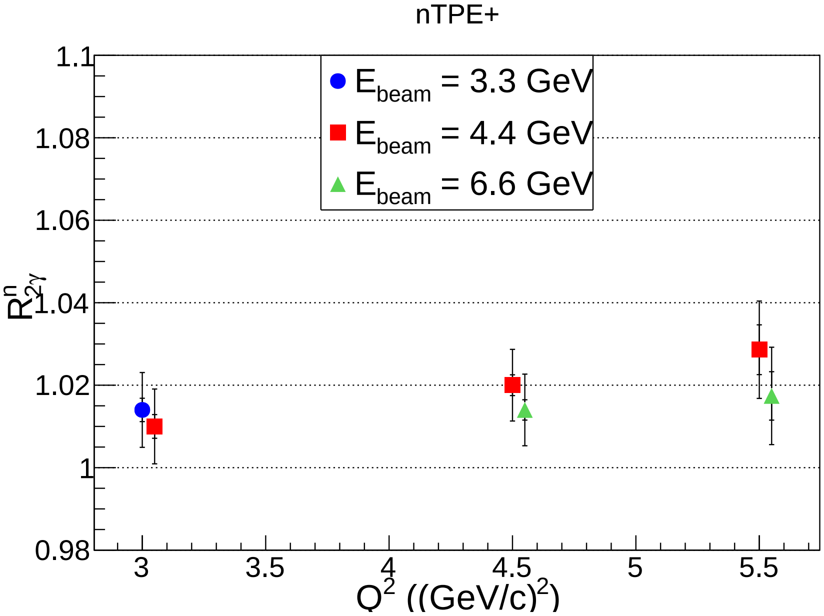

FIG. 8. Projected values of $R^n_{2\gamma}$ plotted as a function of Q^2 for different beam energies: 3.3GeV (blue), 4.4 GeV (red), 6.6 GeV (green), including statistics and systematic uncertainties. The inner error bars is statistics only. The larger error bar shows the total of all systematics.

is presented on Fig. 9. This projection makes the assumption that the discrepancy between the Rosenbluth slope of unpolarized measurements and polarization transfer measurements is uniquely due to two-photon exchange. The *projected* Rosenbluth results (*including nTPE / E12-20-010*, under analysis) are based on the estimation of the ratio $\mu_n G_E^n/G_M^n$ at Q^2=3 and 4.5 $(\mathrm{GeV/c})^2$ from the 2018 global fit from Ye *et al.* [47], and corrected by the estimation of the two-photon exchange from [21]. Theoretical curves shown are the calculations of Ref. [48] (Purple dot-dashed), Ref. [49] (Magenta dot-dashed), the GPD-based model from Ref. [50] (Blue dashed), Ref. [51] (Green dot-dashed), Ref. [52] (Red dot-dashed), and Ref. [53] (Black dot-dashed).

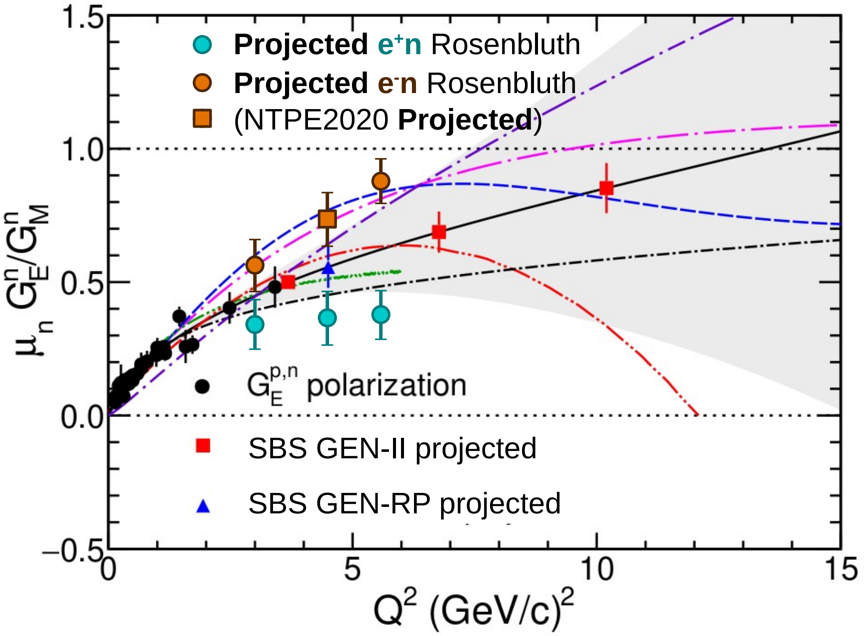

FIG. 9. Projected values of $\mu_n G_E^n/G_M^n$ from our proposed e^+n (cyan bullets) and e^-n (brown bullets) Rosenbluth slope measurements, along with the *projection* of nTPE E12-20-010 (brown square - still under analysis). Shown with this is the projection of upcoming GEn-RP projection [17] (blue triangle) and the *projection* of GEn-II [16] (red bullets - under analysis). Other GEn measurements with polarization function are shown with black bullets. The solid black curve shows the latest global form factor fit from [47]. The other curves are selected models for form factors, detailed in the text.

VII. BEAM TIME REQUEST

This experiment will take place in Hall C utilizing the BigBite spectrometer to detect electrons scattered off the liquid deuterium target, and HCal calorimeter to detect the recoiling neutron and proton. The set of instrumentation for the proposed measurement is identical to the one used in the past GMN/NTPE experiment. We provide a beam estimate our time to measure the ratio of quasi-elastic positron-neutron over quasi-elastic electron-proton cross sections, as well as the Rosenbluth slopes on quasi-elastic positron-neutron and electron-neutron at $Q^2 = 3.0$ (GeV/c)^2, 4.5 (GeV/c)^2, and 5.5 (GeV/c)^2.

We plan to record a total of 468 hours of data with positron beam at $I_{beam} = 1\ \mu$A, including 340 hours on liquid deuterium (LD2) of length $l_{tgt} = 15$ cm and density $d_{tgt} = 0.169$ g.cm^{-3}. The other 128 hours of positron beam will be taken on liquid hydrogen (LH2) of length $l_{tgt} = 15$ cm and density $d_{tgt} = 0.071$ g.cm^{-3} for calibrations and systematic studies. We also plan to take 484 hours of data with electron beam at $I_{beam} = 1\ \mu$A, including 340 hours on LD2, 128 hours on LH2, 16 hours on LH2 combined with a 6% radiation length copper radiator for our neutron detection efficiency measurement, and 16 hours on optics target for calibration. In addition to the beam time, we will also require 32 hours time (two *day* shifts) between each experimental configuration. This duration was the duration achieved during GMn/nTPE, which required a grand total of seven configuration changes. Each configuration change includes the SBS magnet and the hadronic calorimeter (HCal) angle change and the BigBite spectrometer angle and distance change, and also requires a survey of HCal and the SBS magnet. Two of those configuration changes will also require a pass change, which can be done during the magnet reconfiguration. For each kinematic we also require a reconfiguration of the accelerator to go from electrons to positrons. We are working under the assumption that this configuration change can be made in 24 hours, which remains to be confirmed. Table. VII displays a tentative run plan for this experiment. The kinematics of our measurements emphasize the same Q^2 range where TPE in $e-p$ elastic scattering was observed to dominate in Rosenbluth slope. Measuring at this high momentum transfers will provide unique input for testing TPE calculations [21].

[1] R. Hofstadter, Rev. Mod. Phys. **28**, 214 (1956).

[2] M. N. Rosenbluth, Phys. Rev. **79**, 615 (1950).

[3] M. E. Christy *et al.*, Phys. Rev. Lett. **128**, 102002 (2022), arXiv:2103.01842 [nucl-ex].

[4] G. P. Lepage and S. J. Brodsky, Phys. Rev. Lett. **43**, 545 (1979).

[5] G. P. Lepage and S. J. Brodsky, Phys. Rev. Lett. **43**, 1625 (1979).

[6] G. P. Lepage and S. J. Brodsky, Phys. Rev. D **22**, 2157 (1980).

[7] J. Arrington, P. G. Blunden, and W. Melnitchouk, Prog. Part. Nucl. Phys. **66**, 782 (2011), arXiv:1105.0951 [nucl-th].

[8] A. Afanasev, P. Blunden, D. Hasell, and B. Raue, Prog. Part. Nucl. Phys. **95**, 245 (2017), arXiv:1703.03874 [nucl-ex].

[9] B. S. Henderson, L. D. Ice, D. Khaneft, C. O'Connor, R. Russell, A. Schmidt, J. C. Bernauer, M. Kohl, *et al.* (OLYMPUS Collaboration), Phys. Rev. Lett. **118**, 092501 (2017).

[10] J. Arrington, Phys. Rev. C **69**, 032201 (2004).

[11] D. Rimal *et al.* (The CLAS Collaboration), Phys. Rev. C **95**, 065201 (2017).

[12] J. C. Bernauer *et al.* (A1 Collaboration), Phys. Rev. C **90**, 015206 (2014).

[13] A. Schmidt, E. Cline, I. Korover, I. Bernauer, V. Burkert, *et al.*, (2023).

[14] M. Nycz, J. Arrigton, M. Yurov, *et al.*, (2023).

[15] S. Riordan *et al.*, Phys. Rev. Lett. **105**, 262302 (2010).

[16] G. Cates, S. Riordan, B. Wojtsekhowski, *et al.*, unpublished. See `https://www.jlab.org/exp_prog/proposals/proposal_updates/PR12-09-016_pac35.pdf` (2010).

[17] J. Annand, V. Bellini, K. Kohl, N. Piskunov, B. Sawatzky, B. Wojtsekhowski, *et al.*, unpublished. See `https://misportal.jlab.org/pacProposals/proposals/1297/attachments/98337/Proposal.pdf` (2017).

[18] J. Annand, R. Gilman, B. Quinn, B. Wojtsekhowski, *et al.*, unpublished. See `https://www.jlab.org/exp_prog/proposals/09/PR12-09-019.pdf`, `https://www.jlab.org/exp_prog/`

proposals/proposal_updates/PR12-09-019_pac35.pdf (2008).

[19] W. Brooks, G. Gilfoyle, J. Lachniet, M. Vineyard, *et al.*, unpublished. See https://www.jlab.org/exp_prog/proposals/07/PR12-07-104.pdf (2007).

[20] E. Fuchey, S. Alsalmi, and B. Wojteskhowski, "Measurement of the two-photon exchange contribution to the electron-neutron elastic scattering cross section," https://www.jlab.org/exp_prog/proposals/20/PR12-20-010_Proposal.pdf (2020).

[21] P. G. Blunden, W. Melnitchouk, and J. A. Tjon, Phys. Rev. **C72**, 034612 (2005), arXiv:nucl-th/0506039 [nucl-th].

[22] P. Mergell, U.-G. Meißner, and D. Drechsel, Nuclear Physics A **596**, 367 (1996).

[23] G. D. Cates, C. W. de Jager, S. Riordan, and B. Wojtsekhowski, Phys. Rev. Lett. **106**, 252003 (2011), arXiv:1103.1808 [nucl-ex].

[24] C. D. Roberts, M. S. Bhagwat, A. Holl, and S. V. Wright, Eur. Phys. J. ST **140**, 53 (2007), arXiv:0802.0217 [nucl-th].

[25] J. Segovia, I. C. Cloet, C. D. Roberts, and S. M. Schmidt, Few Body Syst. **55**, 1185 (2014), arXiv:1408.2919 [nucl-th].

[26] B. Wojtsekhowski (2020) arXiv:2001.02190 [nucl-ex].

[27] G. A. Miller, Phys. Rev. Lett. **99**, 112001 (2007), arXiv:0705.2409 [nucl-th].

[28] C. E. Carlson and M. Vanderhaeghen, Phys. Rev. Lett. **100**, 032004 (2008), arXiv:0710.0835 [hep-ph].

[29] D. Muller, D. Robaschik, B. Geyer, F. M. Dittes, and J. Horejsi, Fortsch. Phys. **42**, 101 (1994), arXiv:hep-ph/9812448 [hep-ph].

[30] X.-D. Ji, Phys. Rev. Lett. **78**, 610 (1997), arXiv:hep-ph/9603249 [hep-ph].

[31] A. V. Radyushkin, Phys. Lett. **B380**, 417 (1996), arXiv:hep-ph/9604317 [hep-ph].

[32] M. Diehl and P. Kroll, Eur. Phys. J. **C73**, 2397 (2013), arXiv:1302.4604 [hep-ph].

[33] N. Kivel, (2020), private communications.

[34] L. W. MO and Y. S. TSAI, Rev. Mod. Phys. **41**, 205 (1969).

[35] R. Ent, B. W. Filippone, N. C. R. Makins, R. G. Milner, T. G. O'Neill, and D. A. Wasson, Phys. Rev. C **64**, 054610 (2001).

[36] E. B. Hughes, T. A. Griffy, M. R. Yearian, and R. Hofstadter, Phys. Rev. **139**, B458 (1965).

[37] R. G. Arnold *et al.*, Phys. Rev. Lett. **61**, 806 (1988).

[38] L. Durand, Phys. Rev. **115**, 1020 (1959).

[39] E. E. W. Bruins *et al.*, Phys. Rev. Lett. **75**, 21 (1995).

[40] G. Kubon *et al.*, Phys. Lett. **B524**, 26 (2002), arXiv:nucl-ex/0107016 [nucl-ex].

[41] J. Lachniet *et al.* (CLAS), Phys. Rev. Lett. **102**, 192001 (2009), arXiv:0811.1716 [nucl-ex].

[42] K. Kumar *et al.* (MOLLER Collaboration), "The moller experiment: An ultra-precise measurement of the weak mixing angle using møller scattering," (2014), arXiv:1411.4088 [nucl-ex].

[43] P. Souder, J. P. Chen, *et al.* (SoLID Collaboration), "The solenoidal large intensity device (solid) for jlab 12 gev," (2023), arXiv:2209.13357 [nucl-ex].

[44] L. C. Maximon and J. A. Tjon, Phys. Rev. C **62**, 054320 (2000).

[45] P. E. Bosted and M. E. Christy, Phys. Rev. C **77**, 065206 (2008).

[46] M. Sargsian, Private communication (2020).

[47] Z. Ye, J. Arrington, R. J. Hill, and G. Lee, Physics Letters B **777**, 8 (2018).

[48] S. Xu, C. Mondal, J. Lan, X. Zhao, Y. Li, and J. P. Vary (BLFQ Collaboration), Phys. Rev. D **104**, 094036 (2021).

[49] E. L. Lomon, Phys. Rev. C **66**, 045501 (2002).

[50] M. Diehl, T. Feldmann, R. Jakob, and P. Kroll, The European Physical Journal C **39**, 1–39 (2005).

[51] F. Gross, G. Ramalho, and M. T. Peña, Physical Review C **77** (2008), 10.1103/physrevc.77.015202.

[52] J. Segovia, Few-Body Systems **57**, 461–466 (2016).

[53] I. C. Cloët and G. A. Miller, Physical Review C **86** (2012), 10.1103/physrevc.86.015208.

[54] A. Puckett, unpublished. See `https://hallaweb.jlab.org/wiki/index.php/Documentation_of_g4sbs` (2016).

Kin	e^+ or e^-	E_{Beam} (pass) (GeV)	I_{Beam} μA	Q^2 (GeV/c)^2	θ_{BB} / θ_{SBS} (degrees)	target	Time (hours)
Optics	e^-	3.3 (1.5)	10.0	3.0	42.8/29.5	C-foil	16
1-	e^-	3.3 (1.5)	1.0	3.0	42.8/29.5	LD2/LH2	24/12
Reconfiguration to positrons							24†
1+	e^+	3.3 (3*)	1.0	3.0	42.8/29.5	LD2/LH2	24/12
Pass change + BB/SBS magnet configuration change							32
2+	e^+	4.4 (2)	1.0	3.0	28.5/34.7	LD2/LH2	16/16
Reconfiguration to electrons							24†
2-	e^-	4.4 (2)	1.0	3.0	28.5/34.7	LD2/LH2	16/16
BB/SBS magnet configuration change							32
3-	e^-	4.4 (2)	1.0	4.5	41.9/24.7	LD2/LH2	96/16
NDE	e^-	4.4 (2)	1.0	4.5	41.9/24.7	LH2+6% Cu Rad	16
Reconfiguration to positrons							24†
3+	e^+	4.4 (2)	1.0	4.5	41.9/24.7	LD2/LH2	96/32
BB/SBS magnet configuration change							32
5+	e^+	4.4 (2)	1.0	5.5	54.9/18.7	LD2/LD2	120/40
Reconfiguration to electrons							24†
5-	e^-	4.4 (2)	1.0	5.5	54.9/18.7	LD2/LH2	120/40
Pass change + BB/SBS magnet configuration change							32
4-	e^-	6.6 (3)	1.0	4.5	23.3/31.2	LD2/LH2	48/16
Reconfiguration to positrons							24†
4+	e^+	6.6 (3)	1.0	4.5	23.3/31.2	LD2/LH2	48/16
BB/SBS magnet configuration change							32
6+	e^+	6.6 (3)	1.0	5.5	27.6/26.9	LD2/LH2	36/12
Reconfiguration to electrons							24†
6-	e^-	6.6 (3)	1.0	5.5	27.6/26.9	LD2/LH2	36/12
Total beam							**952**
Total time request							**1260**

TABLE VI. Tentative run plan for this experiment, including configuration changes. †: TBC

Appendix A: Detailed Description of the Experimental Setup

1. Parameters of the SBS

The 48D48 magnet from Brookhaven was acquired as part of the Super Bigbite project and will be available for this experiment. It consists of a large dipole magnet which provides a field integral of about 1.6 $\mathrm{T}\cdot\mathrm{m}$, allowing for quasielastic protons to be sufficiently deflected to allow clear differentiation from neutrons. The active field volume has an opening of 46×25 vertical × horizontal), matching the aspect ratio of the neutron arm, and a depth of 48 cm.

The placement of this magnet will be 1.6 m away from the target, which would normally interfere with the beamline. To accommodate this, modifications were made to the iron yoke such that the beamline will pass through the magnet yoke area.

The field configuration will be such that positively charged particles will be deflected upwards away from the hall floor. During the data taking of E12-20-010, we evaluated the optimal SBS field to be 1.12 Tesla-m (which is 70% of the maximum SBS field). For this setting, protons of momentum 3.2 GeV/c are deflected 72 mrad, which translates to a displacement of 0.8 m on HCal, as illustrated on Fig. 4 in the main text. The presence of the magnet also works to sweep low energy charged particles from the target away from the neutron arm. Particles of momentum less than 1.3 GeV/c will be entirely swept outside of the neutron arm acceptance. This greatly reduces the amount of charged low energy background.

2. The BigBite Spectrometer

Scattered electrons will be detected in the BigBite spectrometer. The spectrometer consists of a single dipole magnet (with magnetic field approximately 0.9 T) and a detection system, see Fig. 10, composed of GEM detectors for tracking, a calorimeter for trigger and energy measurement, a timing hodoscope for timing, and a Cherenkov detector for particle identification. The detector package we plan to use for the new experiment is the exact same we have been using for the GMn/nTPE experiments in 2021/2022. We provide details on these detectors in Appendix A.

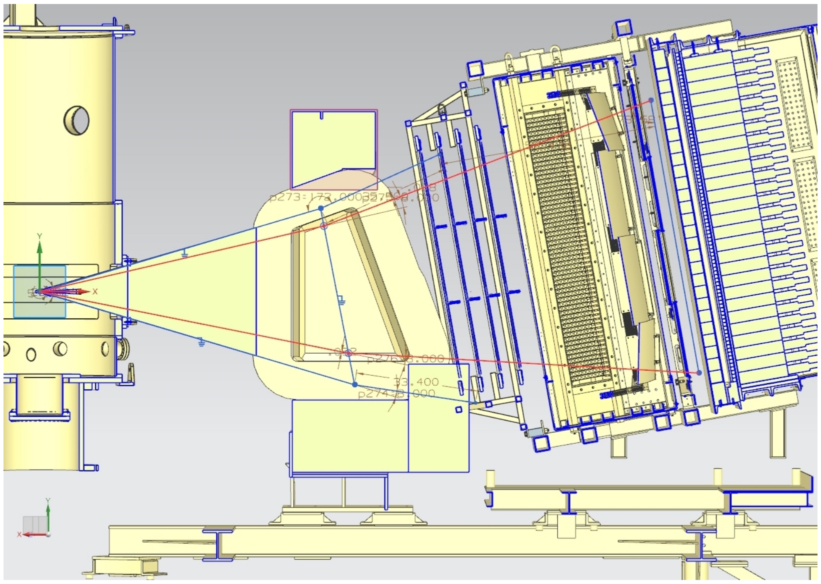

FIG. 10. The BigBite spectrometer with the upgraded detector stack.

a. GEM Chambers

To perform the tracking of charged particles under the high rates anticipated for this experiment, the drift chambers were replaced with gas electron multiplier (GEM) detectors. These detectors have proven to be capable of operating under luminosities of 25 kHz/mm^2 for the COMPASS experiment at CERN. During the data taking of SBS experiments, the spatial resolution of each of these chambers has been observed to be about 100 μm in relatively high background conditions, with their efficiencies being above 90%, as shown on Fig 11. There will be two sets of GEMs placed on each side of the GRINCH Cherenkov detector. The set of GEMs in front of the GRINCH is composed of four layers of GEMs. All four layers were built by the SBS collaborators from UVA.[3] They are composed of a single module

---

[3] Originally two layers of three 40 × 50 cm^2 layers built by the SBS collaborators from INFN were installed. However, issues in their construction meant that they had to be replaced during the GMn experiment.

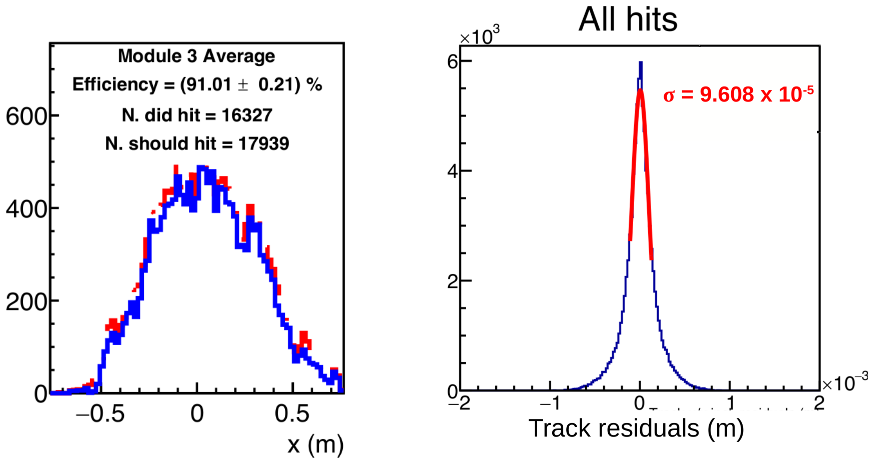

FIG. 11. BigBite GEM efficiency profile for one of the GEM modules (left) and residuals (right).

measuring 40 × 150 cm^2, the long dimension again being vertical and along the dispersive direction. The readout of these modules are oriented in the u/v direction *i.e.* ± 30 degrees with respect to the horizontal direction. The set of GEMs behind the GRINCH has also been been built by the SBS collaborators from UVA. It is composed of a single layer composed of four modules measuring 50 × 60 cm^2 , such that the layer covers 60 × 200 cm^2 (the long dimension again being along the dispersive direction). The readout of these modules are all oriented in the x/y direction.

The background levels in the GEMs have been evaluated, with the help of the G4SBS simulation package ([54] and Sec. 0 b) for the G_M^n experimental readiness review. Those evaluations have been compared with the data taken during GMn/nTPE. Fig. 12 shows the comparison between BigBite GEM occupancies from the GMn/nTPE recorded data and the Monte Carlo simulation, at several beam intensities of 3 μA and 30 μA. At low intensity of 3 μA which is three times the intensity we plan to run, the MC occupancies are in reasonable agreement with the data, and does not represent any challenge. At high intensity, an issue of configuration of the GEM power supply induced a loss of gain correlated with the beam intensity. This issue is illustrated in Fig. 13, which shows the response of the GEMs with different types of power supplies. During GMn/nTPE, the BigBite GEMs were setup with

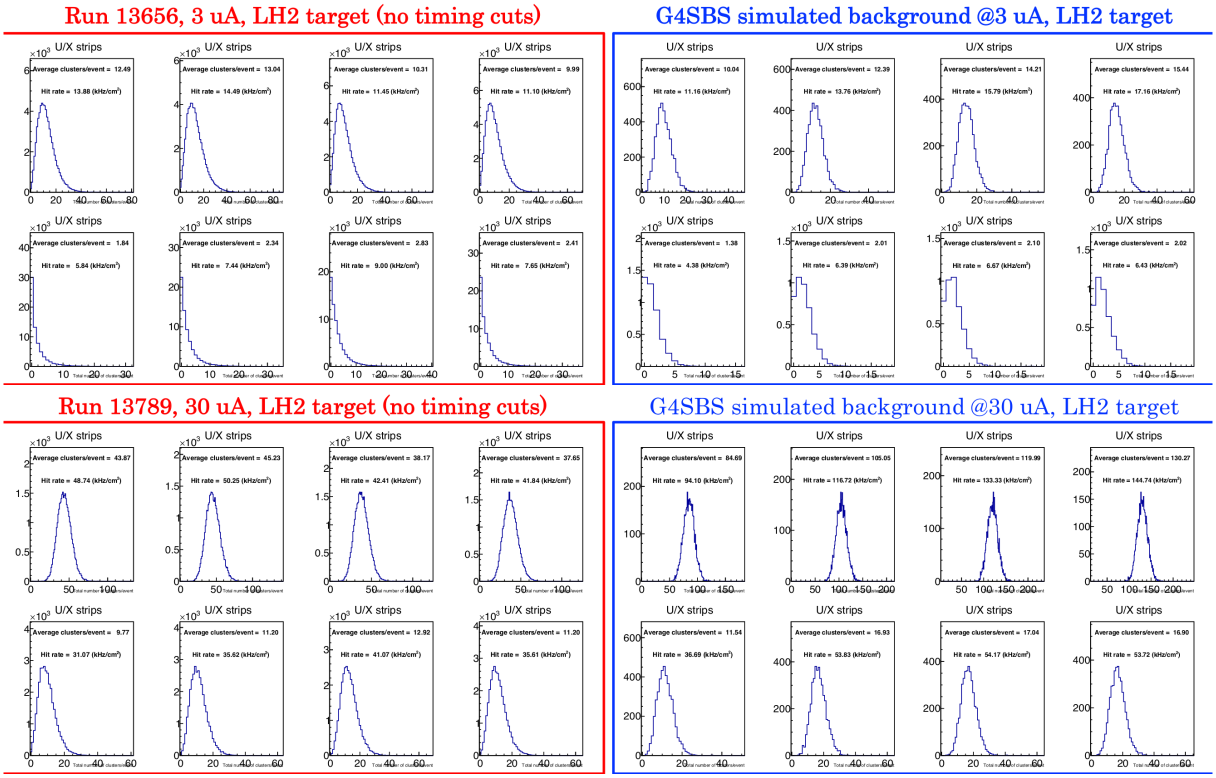

FIG. 12. Comparison between BigBite GEM occupancies from GMn/nTPE data (left plots) and Monte Carlo simulation (right plots), for beam intensity of 3 μA.

the power supply shown by the grey curve. Therefore, their gain/efficiency was dramatically reduced at higher currents.

b. Shower/Preshower

The electromagnetic calorimeter configuration consists of two planes of lead glass blocks which we call the preshower and shower. The preshower, located about 80 cm behind the first GEM chamber, consists of a 2 × 26 plane of 37 cm × 9 cm blocks. The shower, about 1 m behind the first GEM chamber, consists of an 7 × 27 array of 8.5 cm × 8.5 cm blocks. Sums over these blocks form the physics event trigger for the experiment.

The preshower signal can be used to provide an additional method of pion rejection.

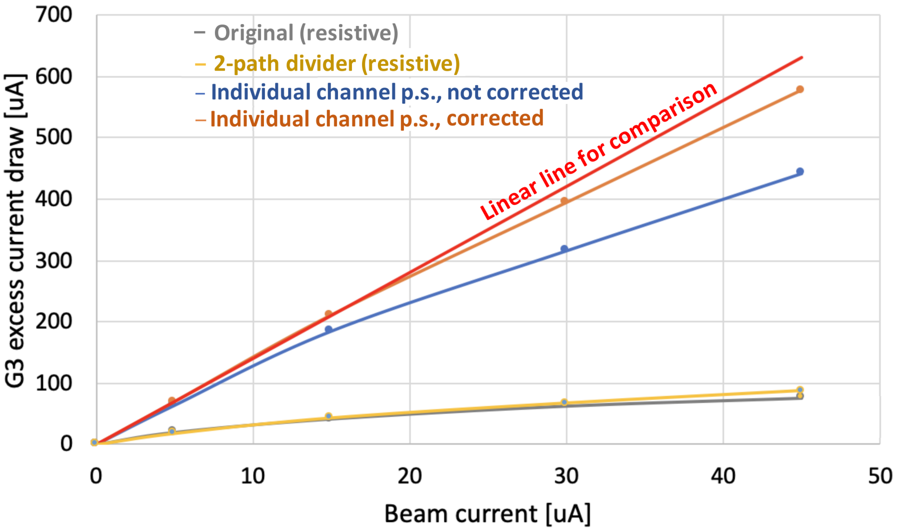

FIG. 13. Comparison of GEM detector setup with different types of power supplies to different beam intensities. The "excess current draw" is a proxy for the detector effective gain. During GMn/nTPE, the BigBite GEMs were setup with the power supply shown by the grey curve.

With sufficient calibration, a pion rejection factor of 1:50 can be achieved by vetoing events with low pre-shower signals. The relative energy resolution for the detector compared to the momentum, shown on Fig. 14 is about $\sigma_{\delta E/p} = 7\%$.

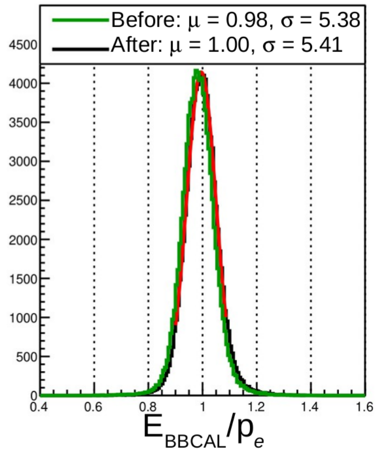

FIG. 14. BigBite calorimeter energy resolution.

c. *Timing hodoscope*

The BigBite timing hodoscope has been built by the SBS collaborators from Glasgow to replace the BigBite scintillator plane and used by all the SBS experiments using BigBite, including GMn/nTPE. It is composed of 90 bars stacked in a plane, each with dimensions 1 in. × 1 in. × 60 cm. The paddle stack will be oriented such that the long dimension of the bars is horizontal *i.e.* perpendicular to the dispersive direction. Signals from the PMTs are processed by NINO front-end cards which, when the PMT pulse crosses the NINO threshold, will produce a digital signal to be read out by CAEN 1190 TDCs which record a leading time and a trailing time. Each of these elements are read out by a PMT on each side, which provides measurement redundancy. This plane is primarily used to provide a signal for nucleon time of flight reconstruction. The analysis of this detector has shown a time resolution of the order of 500 ps, as shown in Fig 15.

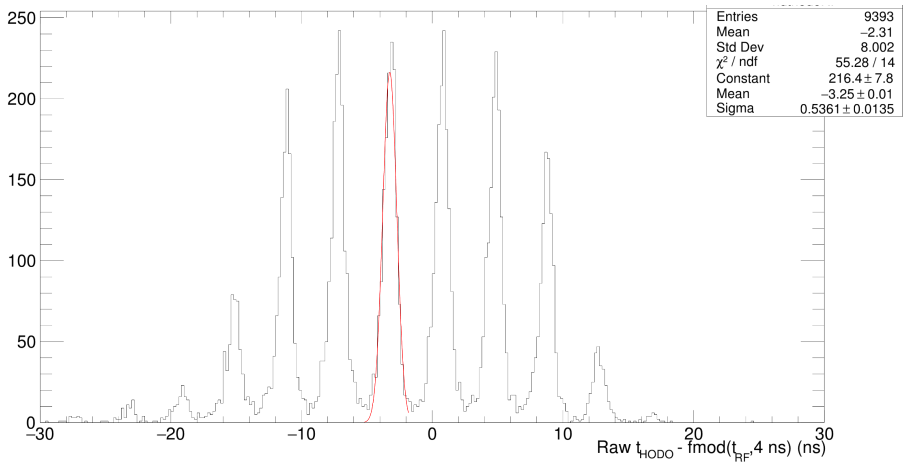

FIG. 15. BigBite hodoscope time from which RF time is subtracted, exhibiting the beam bunch structure. A single beam "bunch" is resolved within 500 ps.

d. GRINCH cherenkov detector

The main purpose of the GRINCH is to provide additional particle identification for offline pion rejection. The GRINCH consists of a tank with a maximum depth of 88.9 cm, with 4 cylindrical mirrors focusing the cherenkov light directly onto a 510 PMT array (60 lines of PMTs, with lines of 9 PMTs alternating with lines of 8 PMTs) placed away from the beam. The radiation gas is C_4F_8, which is an acceptable compromise between light yield for electrons and operating cost. With $n - 1 = 1.35 \times 10^{-3}$, the π threshold is only about 2.7 GeV, so the additional pion rejection will be most effective below this threshold.

Similar to the timing hodoscope, the signals from the GRINCH PMTs pulses are processed by NINO front-end cards which, when the PMT pulse crosses the NINO threshold, will produce a digital signal to be readout by VETROC TDCs, which for each PMT hit will record a leading time and a trailing time. The analog signal will not be recorded however, which means that for each PMT hit, the information of the number of photoelectrons is not directly available (although it can in theory be deduced from the time over threshold).

All of this implies that the electron selection relies on the number of GRINCH PMT firing, instead of relying on the signal amplitude. The position of the PMTs firing can be correlated with the position of the track, as illustrated on Fig. 16 to enhance selection and particle identification.

3. Hadron Calorimeter (HCal)

The Hadron Calorimeter (HCal) has been designed specifically to measure the recoil nucleon for the SBS experiments. Specifically for this experiment (and for G_M^n), HCal combined with the SBS (48D48) magnet provides identification of the recoil nucleon, as well as additional kinematic constraint and possibly timing information on the measured interaction. Nucleon identification is illustrated on Fig. 4. This figure shows the difference between the expected nucleon position in HCal x_{expect} (obtained from the electron information) and the reconstruced HCal cluster position x_{HCal} in HCal, for protons and neutrons. The proton distribution is being shifted upwards by about 0.8 m compared to the neutron.

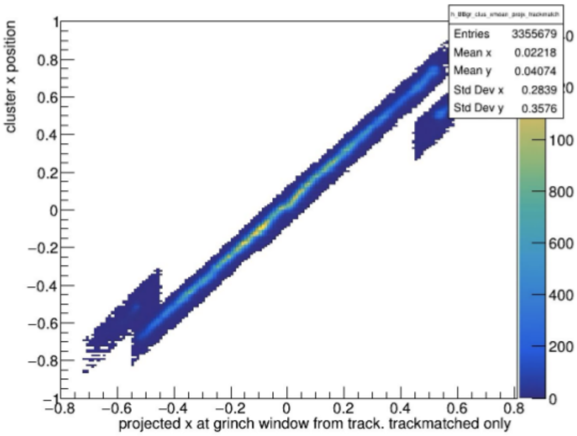

FIG. 16. Correlation between position of GRINCH PMT hits (y-axis) and track position projected at the GRINCH (x-axis). Please note the two "side bands" that corresponds to the side mirrors which deflect the Cherenkov light in a slightly different direction and change the correlation.

The HCal (a CAD model of which is shown in Fig. 17) is composed of 288 modules arranged in an array of 12 × 24. A 3/4 − inchsteel plate is installed just upstream of HCAL,

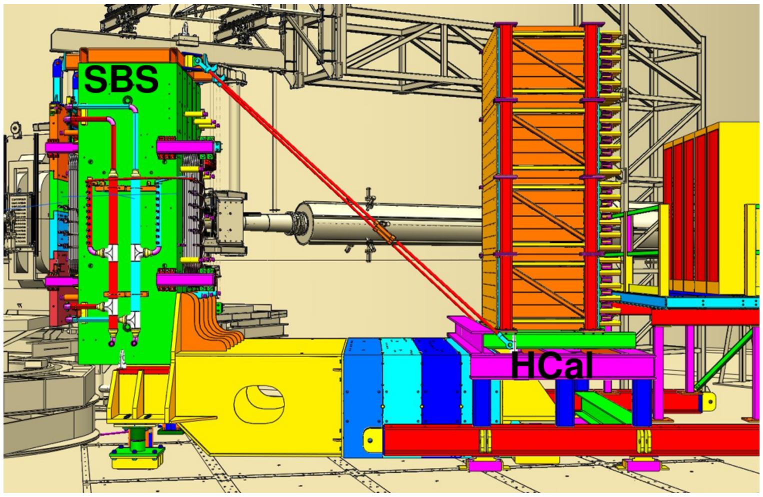

FIG. 17. CAD representation of HCal (right) with the SBS magnet (left)

which serves two purposes:

- initiate the hadronic shower to optimize the calorimeter response;

- shield the modules from a fraction of the low energy secondaries;

Each of these modules measures $6 \times 6\,\mathrm{in}^2$ section, for 3 ft length. They are composed of alternating tiles of scintillators and iron around a central light guide which collects the light generated in the scintillators by the hadronic shower, and guides it to the PMT at the end of the block. Cosmic tests have determined that the average light yield for the HCal modules is around 5 photoelectrons per MeV deposited in the scintillator tiles.

The PMTs are read out with FADC250 which sample the PMT signal every 4 ns and allow to reconstruct the PMT pulse shape, and hence its timing. They are also read out by TDCs which provide additional timing information. Thanks to this, the timing resolution can be about 1 ns. The energy resolution is intrinsically broad due mostly to the small fraction of energy from the hadronic shower actually measured by the scintillator tiles. A thorough discussion on the HCal efficiency is provided in Appendix B.

Appendix B: discussion on HCal efficiency

A crucial parameter for these measurements (both for the past GMn/nTPE and the proposed measurement alike) is the hadron calorimeter efficiency, which is expected to be slightly different for protons and neutrons, and which will contribute to the systematics budget.

a. Evaluation of HCal efficiency in Monte Carlo The efficiency of HCal in the Monte Carlo was evaluated in the following way. Simulations of protons and neutrons were generated over the angular coverage of HCal, and over a wide momentum range from 1 to 9 GeV/c. The energy from the clusters is reconstructed from the simulation as a function of the generated momentum. We evaluate for each momentum the efficiency as the ratio of number of events above a threshold that is 25% of the mean of the cluster energy peak over the total number of events for each momentum. The result is shown on Fig. 18, zoomed in on a momentum range from 2.0 to 5.5 GeV/c. Both proton and neutron detection efficiencies are above 90% for most of the momentum coverage. We also observe a pattern whereby the proton efficiency is larger than the neutron efficiency for momenta up to 5 GeV/c, but dips under the neutron efficiency for higher momenta. One of the current focuses of the ongoing nTPE analysis is the reconciliation between the HCal efficiencies evaluated from Monte Carlo and data, which are currently not in satisfactory agreement (see next).

b. Evaluation of HCal efficiency from data During the nTPE run, we recorded throughout the run elastic H$(e,e')p$ at different SBS magnet settings, in order to keep a strong handle on the HCal efficiency. Indeed, the measurement of the Rosenbluth slope S^n can be affected by the ratio of detection efficiencies of neutron and proton and its corresponding uncertainty. The uncertainty on the ratio of efficiencies can be minimized *as long as we control the stability over the length of the measurement.* This assertion is as valid for the past nTPE/E12-20-010 measurement as it will be for the proposed measurement, which is why we provision hydrogen data taking throughout the run for the proposed experiment. The method to obtain the HCal efficiency from elastic hydrogen is the following: Quasi-electrons electrons are selected among our data sample based on their reconstructed kinematic and other data quality criteria (track fit quality, etc.). Among those N_{el} elastic electron events, the HCal

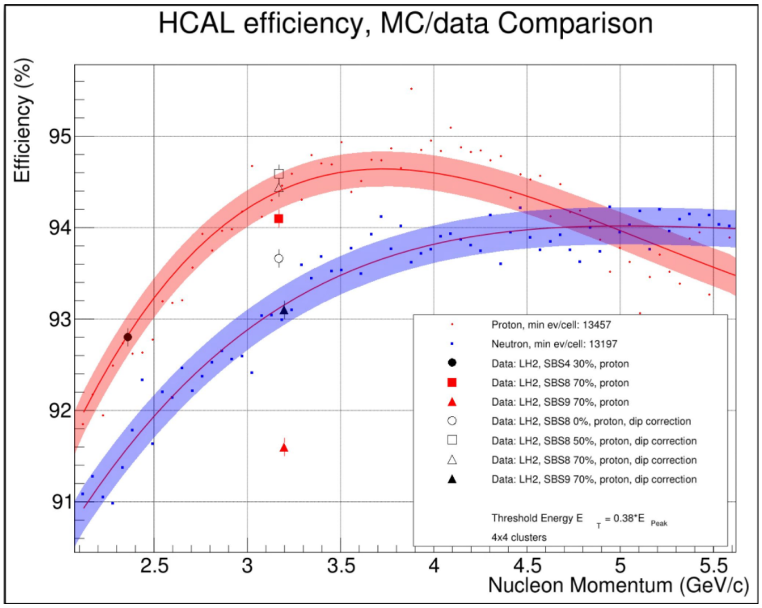

FIG. 18. HCal efficiency as a function of nucleon momentum. The red curves with the red and blue error bands are respectively proton and neutron efficiencies evaluated using Monte Carlo, as described in paragraph 0 a. The markers show the proton efficiency analysis for $Q^2 = 3$ (GeV/c)^{2}and $Q^2 = 4.5$ (GeV/c)^{2}from the 2021-2022 GMn/nTPE LH2 data, as described in paragraph 0 b.

selection is applied, based on the difference between the predicted position x/y_{expect} of the nucleon provided by the electron and the reconstructed position of the nucleon x/y_{HCal}. We note this difference $\Delta x = x_{HCal} - x_{expect}$ and $\Delta y = y_{HCal} - y_{expect}$ in the dispersive and non-dispersive direction respectively. Fig. 19 left illustrates the HCal selection process. The HCal efficiency is then evaluated as the ratio of the number of elastic events N_{det} passing the HCal selection over the total number of elastic events N_{el}. This analysis has been deployed on the GMn/nTPE hydrogen data with several SBS magnetic field settings, in order to cover the full HCal acceptance. The resulting efficiency map from this analysis has been presented on Fig. 19, as a function of x_{expect} and y_{expect}. This map evidences a non-uniformity in efficiency (due to some low efficiency HCal modules), which may be one of the sources of disagreement between the HCal detection efficiency determined with the Monte Carlo and the data. A similar analysis on deuterium has determined that the relative efficiency drop in the "lower efficiency" areas is similar for neutrons and protons. The method that has been

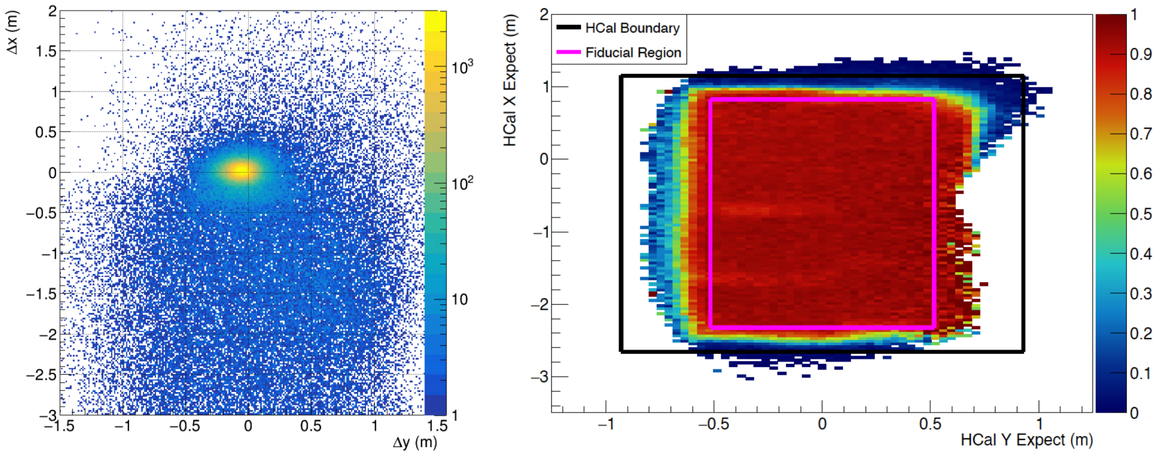

FIG. 19. Left: Difference $\Delta x = x_{HCal} - x_{expect}$ and $\Delta y = y_{HCal} - y_{expect}$ between the expected position of the nucleon provided by the electron $x/y_{expected}$ and the reconstructed position of the nucleon in HCal x/y_{HCal} for Hydrogen data (corrected for the proton deflection). Right: HCal proton efficiency map over the full HCal x_{expect}, y_{expect} coverage, obtained analysis hydrogen data taken over different HCal magnetic fields during the GMn/nTPE experiment.

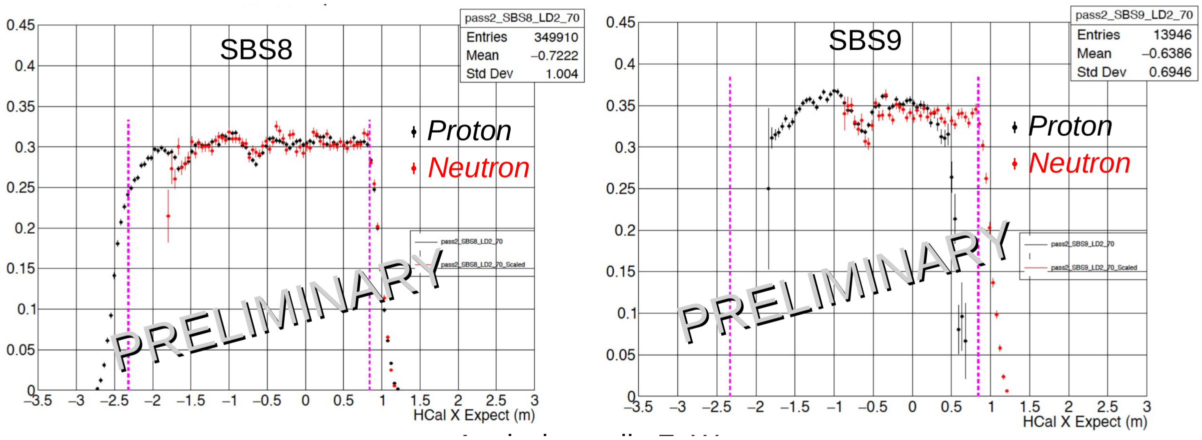

FIG. 20. HCal relative detection efficiency evaluated for protons (black) and neutrons (red) from LD_2 data. Please note the different range in $x_{HCAL,expect}$ from the left plot (SBS8, high energy) to the right (SBS9, low energy).

settled on to correct for this effect is to assign, for both proton and neutron Monte Carlo samples, a weight that correspond to the relative drop of efficiency in the data depending on the expected nucleon position x_{expect}, y_{expect}. Correcting the quasi-elastic proton and neutron Monte Carlo samples with the relative efficiency drop observed in the data corrects the neutron-proton cross section ratios by 0.2 to 0.5% depending on the kinematic.

Appendix C: Simulations, estimations of counting rates and accidentals

The estimates of accidental counting rates have been performed using G4SBS, the GEANT4-based simulation package developed for the SBS experiment [54]. This package includes a wide range of event generators, which allows us to evaluate the rates for both quasi-elastic electron(positron)-proton and electron(positron)-neutron scattering and other reactions such as inelastic electron(positron)-proton and electron(positron)-neutron scattering and inclusive pion production. During the development of the NTPE/E12-20-010 proposal, we had run extensive simulations to show that the trigger rates were manageable, and that the backgrounds were tolerable for the experiment, which was originally planned to run at 30 μA, which is thirty times the luminosity of the positron kinematics for this experiment.

1. Trigger rates

We have evaluated the the trigger rates estimated for our all proposed kinematics. The main processes expected to contribute to the trigger rates for the BigBite spectrometer are:

- the inelastic electron nucleon scattering process;
- photons from inclusive π^0 production;
- and to a lesser extent, charged pions.

Fig. 21 presents the distributions of rate of energy deposit for the different processes involved in the BigBite trigger rates for two kinematics: $Q^2 = 4.5$ (GeV/c)^2, $\epsilon = 0.838$, which is the smallest angle for Bigbite, and $Q^2 = 5.5$ (GeV/c)^2, $\epsilon = 0.420$ which is the largest angle for BigBite but the lowest threshold. For the high (low) energy point, the rates are anticipated to be around 250 (500) Hz at a threshold of 3 (1.3) GeV.

The thresholds to apply to each arm are determined as a function of the elastic peak. For the electron arm, the threshold has been set at $\mu_E - 3\sigma_E$, μ_E and σ_E being respectively the position and width of the fitted elastic peak.

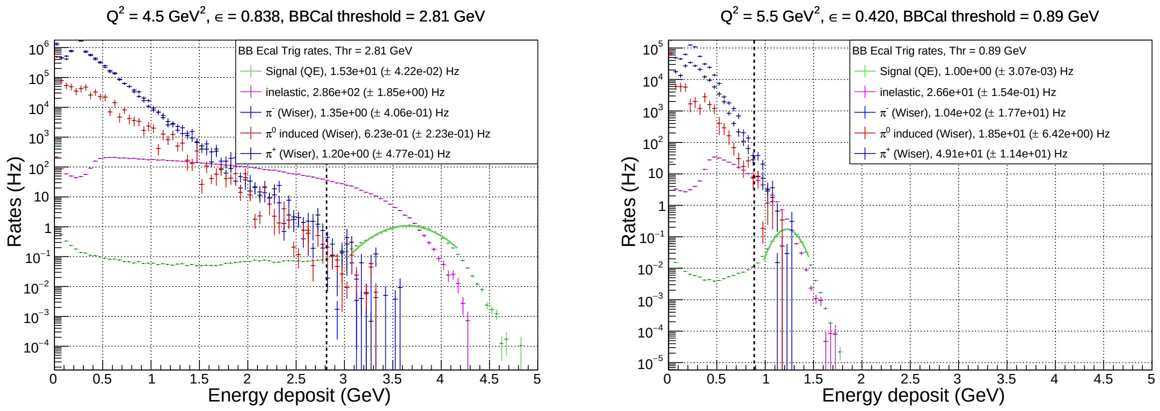

FIG. 21. Rates of the different process contributing to the BigBite electron arm trigger for positrons at $Q^2 = 4.5$ (GeV/c)^2, $\epsilon = 0.838$, which is the smallest angle for Bigbite (left), and $Q^2 = 5.5$ (GeV/c)^2, $\epsilon = 0.420$ which is the largest angle for BigBite but the lowest threshold (right). Quasi-elastic is in green, inelastic in magenta, π^0 in red, π^- in blue, and π^+ in dark blue.

Kin point	threshold (GeV)	Trigger rates (Hz)
1	1.1	355
2	1.8	791
3	1.3	156
4	2.8	305
5	0.9	199
6	2.4	125

TABLE VII. Thresholds and trigger rates for each kinematics with 1μA on 15cm liquid deuterium target.

Those numbers can be compared to the rates observed for nTPE(E12-20-010). For the high energy setting, the BigBite spectrometer was registering 2.8 kHz of triggers at at a threshold estimated around 2.7 GeV for 5.5 μA of triggers. This is to be compared to the 300 Hz at a threshold of 2.8 GeV for 1 μA. Scaling for the luminosity and accounting for a slightly lower threshold, our simulation is off by about 40%. Even accounting for this, our trigger rates remain manageable.